Numerical Modeling of Time-dependent Fluid Dynamics and Differentiation of a Shallow Basaltic Magma Chamber

FRANCISCO GUTIÉRREZ[1]* AND MIGUEL A. PARADA[1]

[1]DEPARTAMENTO DE GEOLOGÍA, FACULTAD DE CIENCIAS FÍSICAS Y MATEMÁTICAS, UNIVERSIDAD DE CHILE, SANTIAGO, 8370450, CHILE

This contribution presents a numerical model of time-dependent physical processes and differentiation in a cooling magma chamber to obtain the magma and liquid composition and model the distribution of minerals and H_2O gas bubbles at any moment and place. The numerical experiments were mainly carried out simulating 10 kyr of differentiation of a 50 km^3 cylindrical stock-like reservoir as one of the end-members of a wide spectrum of magma body geometries. A detailed space–time distribution of compositional varieties and exsolved phases in a chamber of initially superheated basaltic composition (corresponding to a lava of the Hudson Volcano, Chile) was obtained through numerical simulation using the finite-element method. The roof of the chamber is located at 2 km depth in a crust with a geothermal gradient of $30°C/km$. The model considers two spatial directions (z and r) and assumes the magma to be an incompressible non-Newtonian liquid, following the Navier–Stokes formulation, where the density and viscosity depend on the temperature and exsolved solid and volatile phase content, but viscosity also depends on the shear rate. The temperature transfer equation used includes conduction, convection and latent heat. The setting of the model considers that: (1) an extension of 1 km into the country rocks around the chamber imposed on the heat flow across the margins is appropriate; (2) the reaction rates for phase (solid and gas) exsolution correspond to a Gaussian probability function; (3) the involved phases, calibrated from MELTS, are olivine, clinopyroxene, magnetite, plagioclase, orthopyroxene and H_2O gas; (4) the velocity of the exsolved phase movements with respect to the hosting liquid is given by the Stokes' velocity; (5) the sizes of crystals and bubbles in the melt vary in space and time up to a maximum given by the modal crystal size observed in the Hudson Volcano. Our results indicate that the convection dynamics of the reservoir are characterized by three distinct flows of decreasing velocity with time: convective cells, plumes and layer flows along the walls. The along-wall magma flow, which persists during most of the 10 kyr of magma cooling, contributes to the thermal insulation of the chamber interior, giving rise to a nearly permanent coexistence of liquids of contrasting composition. A strong compositional stratification is generated in the upper half of the chamber, with a downward-increasing thickness of layers. Such stratification is mainly the result of continuous upward flow and storage on top of the sidewall residual melts. The lower half of the chamber exhibits an independent convective pattern dominated by ascending plumes. A less pronounced stratification is generated here as a consequence of mixing between the residual liquid in the ascending plumes and the surrounding melt. Crystal accumulations of olivine, clinopyroxene and magnetite at the bottom generate a significant volume of ultrabasic magma at the end of 10 kyr. A plagioclase-rich solidification front along the walls is formed during the last stages of crystallization, when the along-wall magma flow diminishes in velocity. An application of the numerical modeling to a cylindrical sill-like chamber is presented to emphasize the role of the aspect ratio in the magma fluid dynamics, compositional gradients and exsolved phase distribution. The stock-like chamber favors the formation of steep compositional gradients and H_2O gas concentration at the roof. Concentration of the exsolved phases along the margins is favored in a sill-like chamber. From the simulation results, it is possible to infer that stock-like chambers would be more eruptible and would exhibit a wider compositional spectrum of eruptive materials than sill-like chambers. Because solid and liquid dispersion follow different patterns in a convective chamber, the record of crystal–liquid equilibrium would be an exception.

*Corresponding author. Telephone: 56-2-9784111. Fax: 56-2-6963050. E-mail: frgutier@cec.uchile.cl

INTRODUCTION

Most magma bodies exhibit complex zonation attributable to the combined effects of multiple processes involving liquids, solids, and volatile phases. The complexity of these processes has been highlighted in numerous studies providing valuable insights that have greatly contributed to the formulation of the modeling presented in this study. Consequently, we provide here a brief and non-exhaustive review of existing convection models of cooling magma systems and the processes that lead to the observed compositional variations in natural systems.

Crystal settling has been counted as one of the key differentiation processes in natural magma systems since Bowen (1928), giving rise to a mushy zone at the bottom of the storage reservoir (Hills *et al.*, 1983; Tait & Jaupart, 1996). A better understanding of the crystal fractionation mechanism has been obtained from analogue experiments on viscous fluids (e.g. McBirney & Noyes, 1979; Turner & Gustafson, 1981; Huppert & Sparks, 1984; Jaupart *et al.*, 1984; Sparks & Huppert, 1984; Spera *et al.*, 1984; McBirney *et al.*, 1985; Huppert *et al.*, 1986; Jaupart & Brandeis, 1986; Koyaguchi *et al.*, 1990; Thomas *et al.*, 1993; Rao *et al.*, 2002, 2007; Kaneko & Koyaguchi, 2004; Krane, 2004) contributing to the formulation of particle transport-governing laws, particularly permeability (Bergantz, 1995) and hindered settling of solid fractions (Barnea & Mizrahi, 1973; Zhang & Acrivos, 1994; Rao *et al.*, 2002, 2007; Bachmann & Bergantz, 2004). Sidewall crystallization has been considered as an alternative mechanism to crystal settling (see Cawthorn & McCarthy, 1980; Marsh, 1981, 1996; Huppert & Sparks, 1984; Cox & Mitchell, 1988), generating compositional boundary layers (residual liquids) that convect upwards or downwards to the level of appropriate density. Other studies (e.g. McBirney, 1980; Turner, 1980; Huppert *et al.*, 1986; de Silva & Wolff, 1995) have considered sidewall crystallization to be more efficient than crystal settling as a differentiation mechanism, particularly in those chambers with high aspect ratios (height/width). These studies stressed the strong influence of the available length of the sidewall on the efficiency of sidewall differentiation in the production of stratified magma chambers.

Numerous studies on magma chamber evolution, applying numerical analysis, have been carried out, beginning with the work of Shaw (1965), who emphasized the role of thermal and compositional buoyancy in magma convection. Most numerical studies using 1D or 2D approaches (e.g. Brandeis & Jaupart, 1986; Martin *et al.*, 1987; Oldenburg *et al.*, 1989; Bachmann & Bergantz, 2004, 2006; Rüpke & Hort, 2004; Burgisser *et al.*, 2005) have indicated that thermal convection starts to develop from the top of the chamber, assuming that heat is lost predominantly through the roof, whereas compositional convection is triggered by the removal of heavy or light chemical components during crystallization along the walls or bottom of the chamber (Hess, 1972; Morse, 1982; Sparks *et al.*, 1984; Tait *et al.*, 1984). The magma convective regime varies from laminar $(Re < 10^0)$ for crystal mush zones (e.g. Bachmann & Bergantz, 2004, 2006) to turbulent $(Re > 10^3)$ for overheated volatile-saturated basaltic liquids (e.g. Cardoso & Woods, 1999). These regimes and their associated magmatic structures have been thoroughly discussed in numerous studies (e.g. Broadwell & Mungal, 1991; Bergantz & Ni, 1999; Bergantz, 2000; Burgisser *et al.*, 2005; Dimotakis, 2005; Bachmann & Bergantz, 2008).

During the 1990s, the interplay between phase changes and convection was thoroughly studied by means of 2D numerical simulations, including relevant microphysics (e.g. Ni & Incropera, 1995*a*, 1995*b*). An algorithm that considers phase changes and convection in crystallizing binary and ternary systems was obtained from equilibrium phase diagrams and thermochemical and transport data (Oldenburg & Spera, 1990, 1991, 1992*a*, 1992*b*; Spera *et al.*, 1995; Krane & Incropera, 1996, 1997; Krane *et al.*, 1997; Raia & Spera, 1997) emphasizing the role of suspended crystals in chamber zonation and in the style of the convective regime. For example, suspended crystals may stop traveling at a critical volume of solid fraction (Spera *et al.*, 1995; Raia & Spera, 1997), particularly when the cotectic melt composition is reached, giving rise to a zone of crystal mush through which interstitial liquids percolate (Oldenburg & Spera, 1991; Spera *et al.*, 1995). The upward flow of percolated residual liquids is thought to explain the accumulation of crystal-poor liquids in the upper part of the chamber (e.g. Bachman & Bergantz, 2004). Finally, the melt convection regime can be modified by gas exsolution causing density inversion and a subsequent overturn of the magmatic system, facilitating crystal dissolution and thermal rejuvenation of the crystal mush (Burgisser *et al.*, 2005; Bachmann & Bergantz, 2006; Ruprecht *et al.*, 2008).

Most of the 1D and 2D models developed so far point to the formation of stratified magma chambers emplaced in wall-rocks with constant temperature. Crystal settling and descending plumes would give rise to the formation of a crystal-mush zone in the lower levels of the chamber, whereas a solidification front along the margins is thought to generate differentiated liquid that collects at the top of the chamber. Comparisons between simulated chambers and natural examples of closed magma systems are difficult to make, with the exception of a few case studies on zoned felsic and mafic intrusions (e.g. Mahood & Cornejo, 1992; Latypov, 2003*a*), where differentiated magmas have collected along the roof. Most of the compositional variations in plutons have been attributed to

amalgamation of several magma pulses (see Pitcher, 1978; Petford, 1996; Coleman *et al.*, 2004; Glazner *et al.*, 2004; Parada *et al.*, 2005) or to refilling of a magma system involving magma mixing, gas exsolution and thermal rejuvenation. All these processes are far beyond the scope of this study.

The processes involved in the evolution of magmatic systems are far from clear and new approaches are needed. The aim of this study is to generate a time-dependent model that simulates early magmatic processes within a closed magma system emplaced into host rocks that are thermally perturbed by heat transfer from the magma reservoir. The results presented here were obtained by numerical simulations using the finite-element method (FEM; see Appendix A), in an attempt to increase our understanding of the interplay between physical and chemical processes within a cooling magma body. The FEM is a computational method that subdivides an object into very small finite-size elements. Each element is assigned to a set of characteristic equations (see characteristic variables in Appendix B), which are then solved as a set of simultaneous equations to predict the behavior of the object.

The time-dependent numerical model presented here simulates the physical processes of heat transfer, liquid convection, phase exsolution (used hereafter for minerals and gas) and segregation in a closed basaltic chamber hosted in the upper crust, to obtain melt and magma (melt + solid) compositions and distribution of phases at any moment and place during a period of 10 kyr. To simulate a cooling magma system able to produce steep compositional gradients we choose a favorable geometry (column-shaped reservoir) for sidewall differentiation (see de Silva & Wolff, 1995), and an initial melt (superheated basalt) far from a cotectic composition to assess variations in magma fluid dynamics with time. Application of the model to a sill-like chamber is also presented. This contribution also includes videos (see Supplementary Data, available for downloading at http://www.petrology.oxford journals.org) of a stock-like and a sill-like magma chamber that show, amongst others: (1) the variation in space and time of physical (temperature, velocity fields of the liquid phase) and compositional parameters (SiO_2, Mg-number of liquid and liquid + solid) within the magma chamber; (2) the time-dependent temperature variation within the host rocks; (3) the time-dependent phase distribution (solid, liquid and H_2O) within the magma chamber. Additionally, application of the model to a simple binary system (leucite–diopside) is included as Supplementary Data. Unlike the simulation of the early evolution of a complex basaltic system, the simulation of the leucite–diopside system provides an insight into a magma close to its cotectic composition that yields intense crystallization upon small undercooling.

BASIS AND GOVERNING EQUATIONS OF THE MODEL

It is well known that the fluid dynamics of magma chambers are influenced by differences in the density of the liquid phase that result from thermal and/or compositional changes (e.g. Shaw, 1965; Huppert & Sparks, 1984; Brandeis & Jaupart, 1986; Bergantz, 1990; Jaupart & Tait, 1995; Spera, 2000). Several studies (e.g. Chen & Turner, 1980; McBirney, 1980; Sparks *et al.*, 1980; Huppert & Sparks, 1984) have shown that in cooling melts the compositionally induced density differences are larger than the thermal effects on density. The influence of temperature on the liquid density is provided by both heat transfer towards the country rocks during cooling and the latent heat during crystallization. The thermal effect without crystallization provides negative buoyancy to the melt related to liquid contraction, whereas the thermal effect of the latent heat during crystallization slightly expands the residual melt, generating subsequent positive buoyancy. The compositional effect induced by crystallization generally causes positive buoyancy in the melt as a result of the removal of heavy fluid components by crystallization (see Huppert & Sparks, 1984; Spera *et al.*, 1984; Trial & Spera, 1990), whereas the opposite situation occurs in the case of volatile exsolution (Lowenstern, 1994). When the region of mixed crystal and liquid forms a rigid or mushy zone at the margins (Hills *et al.*, 1983), a solidification front starts to develop, armoring the chamber and limiting the eruptibility of the magma at greater than 50 vol. % of crystals (Marsh, 1981, 1996).

The fluid dynamics of a magma is determined by its viscosity (e.g. Shaw, 1965), which in turn depends on the amount of suspended solids, amongst other factors. Aphyric magmas are considered as Newtonian viscous fluids in which the thermal dependence turns the magma into an Arrhenian viscous fluid. The influence of suspended solids on magma viscosity is determined by means of the Einstein–Roscoe equation (Einstein, 1906; Roscoe, 1952; Spera, 2000), which allows the determination of the viscosity of phenocryst-bearing magmas by considering the most efficient packing conditions of the suspended solids (see review by Petford, 2003, 2009). The influence of bubble content and temperature on the relative viscosity of silicate melts has been controversial (Lejeune *et al.*, 1999, 2000; Spera & Stein, 2000; Stein & Spera, 2002; Pal, 2003). Following Stein & Spera (2002) and Pal (2003) we assume that the relative viscosity of bubble-bearing silicate melts is independent of temperature and decreases as the bubble content increases for high capillarity. Shear stress also affects the magma viscosity of a bubble-bearing melt (e.g. Shaw, 1965; Manga *et al.*, 1998). The volatile bubbles may decrease the magma viscosity by orders of magnitude (Stolper, 1982) as a function of the shear stress and capillarity. The non-Newtonian
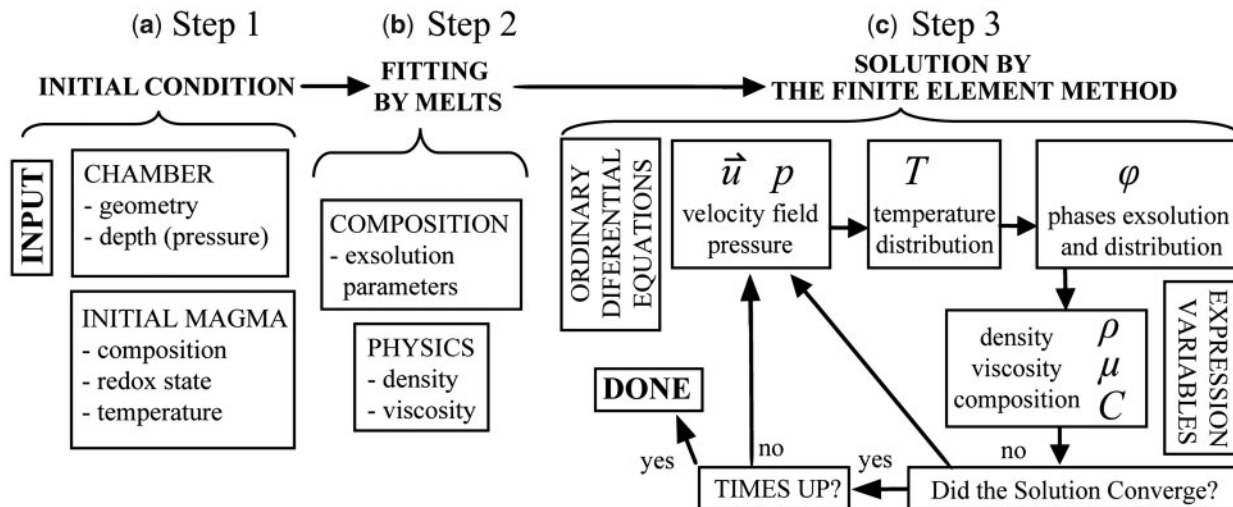
Fig. 1. Flow chart of the model. Step 1, input of the initial conditions; Step 2, set the time-dependent variables of the model including heat transfer, phase exsolution, and magma fluid dynamics; Step 3, solution of the time-dependent differential equations with the finite-element method.

behavior of a melt also depends on the shear stress, and its influence can be determined based on a thermally activated dislocation creep equation. Taking into account that suspended phenocrysts play an important role in the rheology of the magmas, the process of phase exsolution should be considered and the sequence of crystallizing phases calibrated from MELTS (Ghiorso & Sacks, 1995; Asimow *et al.*, 1998).

We define the initial conditions, parameter calibration and governing equations to construct a time-dependent model, which allows a time–space view of convection, phase distribution and liquid composition. Because the evolution of a cylindrical magma chamber is simulated, three independent variables are considered: time (t), radius (r) and depth $(-z)$, where r and z correspond to cylindrical coordinates, assuming axial symmetry around the z axis. Axial symmetry is common for cylindrical 3D geometries. If the geometry is axisymmetric, any variable depends on the radial (r) and vertical (z) direction but not on the angular (θ) direction. Hence, it is possible to solve a 2D problem in the r–z plane instead the full 3D model, saving memory and computation time. For 2D axisymmetric models, COMSOL Multiphysics can compute any integral of volume and surface by multiplying the integrand by $2\pi r$ prior to integration.

Three steps for the numerical modeling were defined (Fig. 1). Step 1 corresponds to the input of the initial conditions defined for this model. Step 2 is designed to set the expression variables to be used in the model, including heat transfer, phase exsolution and magma fluid dynamics. Step 3 corresponds to the solution of the time-dependent equations by means of the FEM.

Initial conditions correspond to the initial values for the dependent variables of the processes to be modeled. In our case, the initial conditions are the depth (pressure) of the magma chamber and the composition, temperature and redox state of the initial melt. The setting of the model consists of the assignation of values for each expression variable, which in turn are temperature-dependent. Viscosities, densities, heat capacities, and fractions of the phase and liquid compositions were calibrated from MELTS (R.5 Ghiorso & Sacks, 1995; Asimow *et al.*, 1998). Finally, we use the Multiphysics software R.3.4a to obtain the solution of the governing equations by the FEM method. The mesh of elements comprises more than 10 000 triangular finite elements using a static mesh, or Eulerian description.

Heat transfer

The heat balance equation to obtain the temperature of the magma considers conduction, convection and latent heat and is given by

$$
\sum_{j}^{N+1} \rho_j Cp_j \left(\frac{\partial T}{\partial t} + \vec{u} \cdot \nabla T \right)
$$
$$
= \sum_{j}^{N+1} k_j \nabla^2 T + \sum_{j}^{N} \rho_j qL_j \left(\frac{\partial \phi_j}{\partial t} + \vec{u}_j \cdot \nabla \phi_j \right) \tag{1}
$$

where j designates the phase, N is the number of exsolved phases, ρ is the density, Cp is the heat capacity, T is the temperature, k is the thermal conductivity, ϕ is volume fraction of the phase, $\vec{u}$ is the phase displacement velocity, and qL is the latent heat related to phase changes. In this

perfect mixing thermal formulation the exsolved phases contribute to the thermo-physical properties of the magma, but they do not extract energy from it. The heat transfer into a H_2O-free country rock beyond the margin of the chamber is obtained from

$$\rho_r Cp_r \frac{\partial T_r}{\partial t} = k_r(z, T_r)\nabla^2 T_r \qquad (2)$$

where ρ_r is the density, Cp_r is the heat capacity, T_r is the temperature, and k_r is the thermal conductivity of the rock. The heat conduction through the country rock reproduces the evolution of temperature in the host rock around the chamber without considering hydrothermal circulation. k_r is a temperature- and depth-dependent parameter and is given by the Chapman & Furlong (1992) expression

$$k_r = k_r^0(1 + 1.5 \times 10^{-3}z)/(1 + 10^{-4}T_r) \qquad (3)$$

where k_r^0 is the thermal conductivity at depth $z = 0$. Despite the fact that the effect of temperature on the thermal conductivity of the host rock is small, we include it to further assess the thermal isolation of the chamber.

Because temperature discontinuities along the margins of the chamber produce oscillations in the FEM results, we assume that the walls are not perfect conductors. For that reason we use a heat flux across the margin of the chamber (q_r), given by the temperature difference between the magma (T) and the country rock (T_r), which triggers phase exsolution and convection (Brandeis & Jaupart, 1986; Martin et al., 1987). The heat flux is given by the Neumann boundary condition

$$q_r = \vec{n} \cdot k_r \nabla T = \frac{k_r}{L_r}(T - T_r) \qquad (4)$$

where $\vec{n}$ is the vector normal to the chamber boundary and L_r is the distance in the country rocks from the reservoir walls, imposed on the heat flux (q_r) to allow its thermal effect to develop. The initial temperature of the country rocks and the border temperature conditions far away from the chamber are given by

$$T_r = T_r^0 - G_r z \qquad (5)$$

where T_r^0 is the ground surface temperature and G_r is the geothermal gradient. We heuristically estimate that the thermal influence of the chamber is null at 8 km from the walls. Beyond this the host-rock system is adiabatic.

Exsolution of phases and magma compositions

Most numerical models of solidification of magmatic systems or metal alloys, which include the subsequent redistribution of the component and the convective liquid segregations, are self-consistently based on thermodynamic equilibrium (e.g. Krane & Incropera, 1997; Krane et al., 1997; Raia & Spera, 1997). In other words, the state variables (temperature, pressure, oxidation state, phase composition, etc.) are derived from the chemical and thermodynamic equilibrium. To simulate phase exsolution and the liquid compositions in a more complex magmatic system such as a natural basalt, we present a new model of exsolution, in which the volume fraction of the exsolved phases (ϕ_j) are explicit functions of temperature only. Consequently, ϕ_j varies with time as follows:

$$\frac{\partial \phi_j}{\partial t} + \vec{u}_j \cdot \nabla \phi_j = -Q_j\left(\frac{\partial T}{\partial t} + \vec{u}_j \cdot \nabla T\right) \qquad (6)$$

where $\vec{u}_j$ is the exsolved phase movement velocity, and Q_j is the phase exsolution rate. It should be noted that the exsolved phases segregate from a flowing melt is thus

$$\vec{u}_j = \vec{u} + \vec{u}_j^{SV} \qquad (7)$$

where u is the liquid movement velocity and u_j^{sv} is the phase segregation velocity. An artificial diffusion term is added to the convection-dominated transport of the phases to suppress oscillation instabilities caused by the discretization involved in FEM. Formation of chilled (glassy) margins to the chamber is also not considered in the model.

The exsolution rate with respect to temperature of each j-phase (solid and H_2O) from the liquid is adjusted by a Gaussian probability function that depends on liquid temperature:

$$Q_j = -\frac{\phi_j^f}{\sqrt{2\pi}\sigma_j}\exp\left(-\left(T - T_j^m\right)/2\sigma_j^2\right) \qquad (8)$$

where ϕ^f, T^m and σ are the final volume fraction of the j phase and the mean and standard deviation of the exsolution temperature, respectively. The parameters ϕ^f, T^m and σ can be calibrated from data obtained from self-consistent models (e.g. MELTS, binary and ternary systems). The solution for ϕ_j incorporates the variable of states included in the selected self-consistent model (MELTS in this case).

Considering steady-state integration of the ϕ_j equation, the phase volume fraction of the j phase that crystallizes (or exsolves) at T from each residual liquid (ϕc) is obtained from the following error functions:

$$\phi c_j(T) = \frac{\phi_j^f}{2}\left(\mathrm{erf}\left(\frac{T - \mu_j}{\sqrt{2}\sigma_j}\right) - \mathrm{erf}\left(\frac{T^m - \mu_j}{\sqrt{2}\sigma_j}\right)\right). \qquad (9)$$

Because temperature varies with time and position [equation (1)], the above expression allows the location of the residual liquid that exsolved a specific phase volume fraction to be obtained.

The volume fraction of the residual liquid is

$$\phi_l = 1 - \sum_{j}^{N} \phi_j. \qquad (10)$$

Neglecting both assimilation of country rock and solid-liquid re-equilibration (i.e. no thermal energy is transferred across the crystal–liquid interface), the

composition of the liquid phase (C_l) and that of the whole magma (C_m) can be obtained directly by mass balance using the phase volume fraction

$$C_l \rho_l \phi_l = C_m^0 \rho_m^0 - \sum_{j}^{N} C_j \rho_j \phi c_j \qquad (11a)$$

$$C_m \rho_m = \sum_{j}^{N+1} C_j \rho_j \phi_j \qquad (11b)$$

where C_m^0 and ρ_m^0 are the composition and density of the initial liquid, respectively. It should be noted that in the model the liquid and magma composition are expression variables, which depend on the content of each exsolved phase. Because the liquid and magma composition are not differential variables the diffusion of components has been neglected (Fick's Law is not applicable). This limitation does not substantially affect the resulting composition because diffusion velocities are 10^4 times lower than liquid convection in the early state of the magma chamber.

The closed magma chamber considered in this model requires insulation conditions for the exsolution of the phases, given by

$$\vec{n} \cdot \left(\phi_j \vec{u}_j \right) = 0. \qquad (12)$$

In summary, the proposed phase exsolution model allows us to obtain, from the temperature of exsolution, the volume fraction of the exsolved phases as well as the phase volume fraction that has been exsolved from any residual liquid. Additionally, it is possible to determine the liquid and magma composition without using partial differential equations for each chemical component.

Magma fluid dynamics

In the fluid dynamic model of the magma, we include: (1) the governing equation of the velocity field of the magma; (2) the parameters controlling the changes in viscosity; (3) crystal radius.

The model presented here does not take magma compressibility into account because the solution of the magmatic system would depend on the visco-elastic deformation of the wall-rocks, which is beyond the scope of this study. This limitation will be considered in a further study. The incompressible non-Newtonian assumption of our analysis implies that pressure varies linearly along the chamber walls. There are two momentum equations and one continuity equation, which are assembled in the incompressible Navier–Stokes formulation:

$$\rho_m \left(\frac{\partial \vec{u}}{\partial t} + \left(\vec{u} \cdot \nabla \right) \vec{u} \right) = \nabla \cdot \left(\mu \left(\nabla \vec{u} + \nabla \vec{u}' \right) \right) - \nabla p - \rho_m \vec{g} \qquad (13)$$

$$\nabla \vec{u} = 0 \qquad (14)$$

where ρ_m is the magma density, $\vec{g}$ is the gravity acceleration vector, $\vec{u}$ is the liquid velocity; p is the pressure, and μ is the dynamic viscosity. Because both ρ_m and μ are functions of the temperature and exsolved phase fraction, the model considers the time-dependent variations of these magma properties [see equations (1) and (6)]. The incompressible character is defined by the continuity equation, whereas the density of the magma is obtained from

$$\rho_m = \sum \phi_j \rho_j. \qquad (15)$$

The density of the liquid is given by a fifth-order polynomial function of T, including the thermal and compositional effects on liquid density calibrated from MELTS:

$$\rho_l = P^5(T) = \sum_{i}^{6} a^i T^i. \qquad (16)$$

Because the effective magma viscosity (μ) of a non-Newtonian fluid depends on temperature (T), solid and gas content (ϕ_s and ϕ_g) and shear rate ($\dot{\gamma}$), we use an expression for μ that includes the influence of these variables by considering four functions:

$$\mu = \mu_T \mu_s \mu_g \mu_{sr} \qquad (17)$$

where μ_T is an Arrhenian expression for the influence of temperature on the liquid viscosity, μ_s and μ_g are Einstein–Roscoe-type functions used for solids and gas, respectively, and μ_{sr} is a dislocation creep expression. The model accounts for simultaneous, position-dependent, Newtonian and non-Newtonian magma rheology by considering the continuum transition of μ between crystal-poor liquids and crystal-rich melts as well as the continuum effects of temperature and shear rate on the viscosity of any magma. However, the model does not account explicitly for changes in magma rheology by modifying the partial differentiation equation structure and its boundary conditions.

The Arrhenian expression for μ_T used here is a simplification of recent experimental results on silicate melts showing that the influence of temperature on viscosity for a wide temperature interval (1000°C) is non-Arrhenian (eg. Hess et al., 1996; Giordano & Dingwell, 2003; Russell et al., 2003). By using a non-Arrhenian law (Tammann–Vogel–Fulcher equation) to adjust the temperature influence on μ for a restricted temperature interval (300°C), the non-Arrhenian parameter obtained is approximately zero. The functions are

$$\mu_T = \mu^0 \exp\left[\frac{Ea}{R} \left(\frac{1}{T} - \frac{1}{T^0} \right) \right] \qquad (18)$$

$$\mu_s = \left(1 - \frac{\phi_s}{\phi_s^0} \right)^{ns} \qquad (19)$$

$$\mu_g = \left(1 - \frac{\phi_g}{\phi_g^0}\right)^{ng} \tag{20}$$

$$\mu_{sr} = [1 + \dot{\gamma}]^3 \tag{21}$$

where μ^0 and T^0 are the initial viscosity and temperature, respectively; Ea is the activation energy of the Arrhenius law, R is the ideal gas constant, ϕ_s^0 and ϕ_g^0 are the maximum packing values for solids and bubbles (prior to coalescence), respectively, ns ($<$0) and ng ($>$0) are the exponents for solids and gases of the Einstein–Roscoe equation, and $\dot{\gamma}$ is the shear rate used in the dislocation creep equation. Here we use $ng > 0$ to reproduce the decrease of μ caused by increased gas content. Although coalescence is an efficient transport mechanism of gas–water in magma systems (e.g. Shinohara *et al.*, 1995), it is not considered in the gas distribution of this model.

We recover the shear rate by

$$\dot{\gamma} = \sqrt{\frac{1}{2}\left(4\frac{\partial u^2}{\partial r} + 2\left(\frac{\partial u}{\partial z} + \frac{\partial v}{\partial r}\right)^2 + 4\frac{\partial v^2}{\partial z} + 4\left(\frac{u}{r}\right)^2\right)}. \tag{22}$$

Despite the fact that the effect of dislocation creep on the viscosity is low, we included it because of the non-Newtonian character of the magma assumed here. On the other hand, the steady-state relative displacement of the exsolved phases with respect to the liquid, regardless of the upward or downward movement of magma pulses, is determined by the Stokes' settling velocity law ($\vec{u}_j^{SV}$):

$$\vec{u}_j^{SV} = \frac{2}{9} r_j^2 g \frac{\left(\rho_l - \rho_j\right)}{\mu} \hat{z} \tag{23}$$

where $\hat{z}$ is the vertical unitary vector and r is the mineral and bubble radius, which is determined by the exsolved phase volume fraction

$$r_j = \min\left(r_j^0 \frac{\phi_j}{\phi_j^f}, r_j^0\right) \tag{24}$$

The effective viscosity of the magma [equation (18)] is included in equation (23) so that the settling velocity accounts for the retarding or advancing effect of the temperature, crystal and bubble concentrations and shear rate. This approach is comparable with those predictions of the hindered settling velocities that use the viscosity of liquid corrected by a factor $f < 1·0$ that depends on the crystal fraction (Barnea & Mizrahi, 1973; Zhang & Acrivos, 1994; Rao *et al.*, 2002, 2007; Bachmann & Berbantz, 2004). The variation of the magma viscosity with crystal content is determined by the Einstein–Roscoe equation and f corresponds to

$$f = 1/\mu_s \tag{25}$$

Figure 2 shows a comparison between the variations of f as the volume concentration of crystals increase, obtained from our formulation and those of other workers.

Because the effective viscosity increases during magma cooling and crystallization towards the chamber walls, the Faxén correction to account for the retarding effect of the reservoir walls on phenocryst Stokes' velocity (Kahle *et al.*, 2003) is not included. In the spherical approach we use, there is a critical radius (r^0) for crystals and bubbles over which nucleation increases instead of crystal and bubble growth. Provided that r is a linear function of ϕ_j such a radius would also depend on T by accumulative error functions. Because the habits of olivine and pyroxene (the main fractionating minerals in our simulation) do not commonly exhibit substantive differences between short and long crystal axes, the Stokes' velocity of suspended crystals was not corrected for shapes deviating from spheres (Le Roux, 2004).

Liquid flow along the chamber walls is controlled by the no-slip boundary condition in an insulated chamber (no volume of magma penetrates beyond the walls). In other words, we assume that the melt does not flow across the wall–liquid interface:

$$\vec{u} = 0. \tag{26}$$

Despite the fact that we imposed the boundary condition of no-slip only along the walls, $\vec{u} = 0$ in the interior of the chamber also occurs at the interface of two convective fluids with an opposite sense of displacement.

INITIAL CONDITIONS AND PARAMETER CALIBRATION FOR THE EXPERIMENTS

The initial composition (Table 1) of the magma corresponds to that of a homogeneous calc-alkaline basalt from the Hudson Volcano in the Patagonian Andes (Gutiérrez *et al.*, 2005). We chose 2 wt % of H_2O for the initial melt, which is consistent with the 2–6 wt % reported for many arc basalts (e.g. Sisson & Grove, 1993; Murphy *et al.*, 2000; Couch *et al.*, 2001; Pichavant *et al.*, 2002; Cervantes & Wallace, 2003; Gurenko *et al.*, 2005), although an elevated H_2O content of $>$8 wt % (Carmichael, 2002, 2004; Grove *et al.*, 2002) has been estimated, prior to degassing resulting from either eruption or magma ascent from the source. This non-primitive basalt would have originated from a deep crustal hot zone near the Moho (*c.* 35 km depth) where the first stage of magma differentiation is thought to occur (Annen *et al.*, 2006). This model assumes that the initial basalt is superheated at 1200°C, which is likely to occur when magmas rise adiabatically because the corresponding decompression curve is by far steeper than the H_2O-deficient basaltic liquidus.
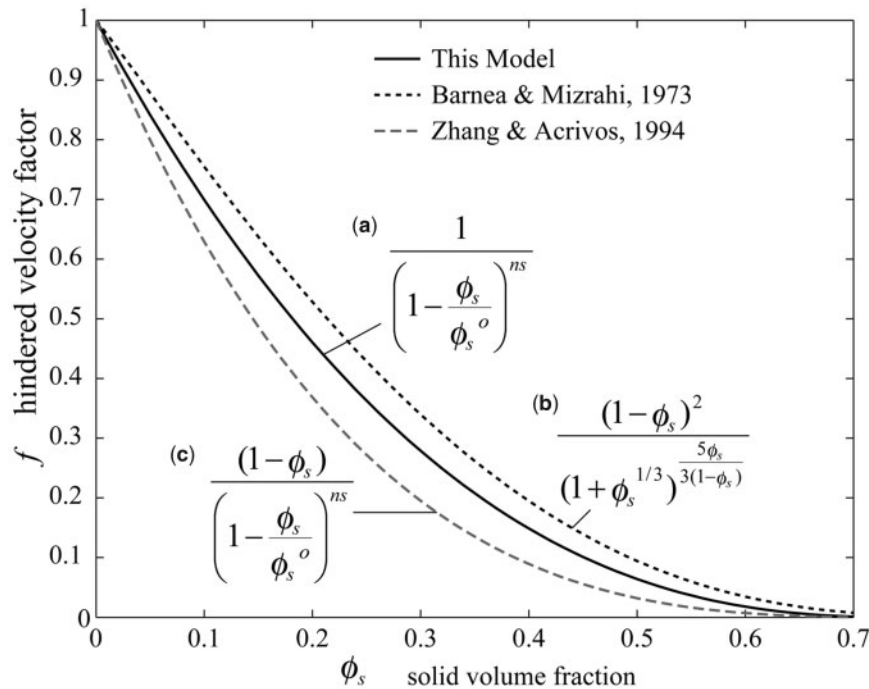
Fig. 2. Variations of the hindered settling function (f), according to different researchers, as the volume fraction of crystals (ϕ_s) increases. Curves: (a) this model; (b) Barnea & Mizrahi (1973); (c) Zhang & Acrivos (1994).

Table 1: Initial composition of the magma

Component	wt %
SiO_2	48·3
TiO_2	1·3
Al_2O_3	17·9
FeO	5·3
Fe_2O_3	4·0
MnO	0·1
MgO	6·8
CaO	10·0
Na_2O	3·6
K_2O	0·4
P_2O_5	0·2
H_2O	2·0

This composition corresponds to a basalt sample of the Hudson Volcano Complex (45·5°S, 72·5°W) in the southernmost volcano of the Southern Volcanic Zone of the Andes (Gutiérrez *et al.*, 2005).

The numerical model presented in this study attempts to reproduce the evolution of a basaltic magma chamber during 10 kyr of cooling and crystallization. This interval is considered appropriate for showing the main processes that take place during the early stage of evolution of a small basaltic magma reservoir. In fact, following the magma chamber cooling time expression given by Hawkesworth *et al.* (2000), we obtain 10 kyr for a degree of crystallization of 50 vol. % (76 wt %) for a basalt reservoir (basalt density $2600 \, kg/m^3$, basalt heat capacity $1500 \, J/kg \, K$, latent heat $4 \times 10^5 \, J/kg$) that cools by 180°C with a geothermal power output of 500 MW. Because the geometry of the Hudson magma reservoir is not known, a chamber of 50 km^3 ($r = 2 \, km$; height $= 4 \, km$) with an aspect ratio (height/width) of 1·0, simulating a column-shaped stock-like body, was assumed (Fig. 3). This geometry represents one of the end-members (stock-like body) of a wide spectrum of potential magma body geometries including sills, laccoliths (aspect ratio lower than 1·0) and dikes (aspect ratio higher than 1·0). The influence of the aspect ratio of the chamber is important with respect to its compositional evolution (see McBirney, 1980; Turner, 1980; Brandeis & Jaupart, 1986; de Silva & Wolff, 1995). Chambers with high aspect ratios (column shaped) have long vertical walls along which upward and downward magma transference operates efficiently. Additionally, this geometry would promote sidewall crystallization, subsequent buoyant boundary layer formation and thermochemical convection that gives rise to more pronounced compositional stratification than coin-shaped chambers (low aspect ratio). The modest volume of magma chosen for the model is comparable with a magma body formed
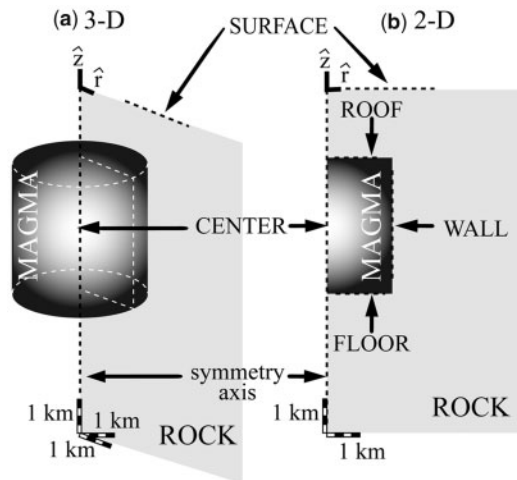
Fig. 3. Geometry of the selected magma chamber: (a) Cylindrical magma chamber of $50\,km^3$ simulating a column-shaped stock-like body; (b) cross-section of the right half of the magma chamber that is used to show the simulation results in Figs 6–8 and the videos.

in a single pulse of emplacement, without further refilling or evacuation of magma (closed system). The roof of the chamber is located at 2 km depth in continental crust with a geothermal gradient of 30°C/km. An extension of 1 km (L_r) in the country rocks around the chamber is imposed on the heat flow across the margins and is based on the expected extension of the H_2O-free contact aureole around intrusions of similar size. The thermal structure of the country rocks is calculated up to 8 km away from the contact using the thermal conductivity of rocks given by Chapman & Furlong (1992) without considering an H_2O circulation system. Although the H_2O-free country rock assumption is unrealistic, a number of magma chambers beneath basaltic volcanoes and gabbroic column-like stocks are hosted in fine- to medium-grained isotropic granitoids exhibiting very low primary porosity. Consequently, H_2O circulation is mainly restricted to deep secondary structures. Examples of modern volcanic edifices built over granitoid batholiths in the Andes of south–central Chile are the Villarrica, Choshuenco, Puyehue, Calbuco and Hudson volcanoes, amongst others (e.g. López-Escobar et al., 1995; Sepúlveda et al., 2004; Gutiérrez et al., 2005).

Variations in the physical properties and compositional parameters of the magma are calibrated for a cooling interval between 1200°C and 900°C when less than 5% of its volume remains liquid. For magma below 900°C such variations were neglected. The values of the constants required to obtain the physical and compositional parameters used in the model are shown in Tables 2–4. The physical parameters of the melts (ρ_m and μ), as well as the thermal (Cp and qL) and compositional

parameters of the exsolved phases and residual liquids (ϕ^f, T^m, and σ) were calibrated using the MELTS software (R.5, Ghiorso & Sacks, 1995; Asimow et al., 1998) at 100 MPa and an oxygen fugacity buffered at QFM + 3 log units (where QFM is the quartz–fayalite–magnetite buffer). On the other hand, the incompressible assumption of the Navier–Stokes's formulation implies that pressure varies linearly through the 4 km high chamber from 55 to 165 MPa. However, its effects on the physical and compositional properties of the magma are neglected. The variations of the magma properties and compositions are functions that depend on differential variables such as temperature, crystal and gas content, etc. Because temperature varies in time and space, ρ_m and μ, as well as the calibrated compositional parameters, do so concomitantly during the simulations (see Figs 4 and 5). We obtained k (thermal conductivity) for each participating mineral from the compilation of Clauser & Huenges (1995). The calibration indicates that a liquid at 900°C has exsolved c. 76% of solid phases (Fig. 5d), distributed as follows: 4% olivine, 13% clinopyroxene, 4% magnetite, 3% orthopyroxene, 51% plagioclase, and nearly 1% of accessory minerals. The H_2O exsolved from the same liquid occupies c. 23 vol. %. The maximum radii of the exsolved phases are given in Table 3 and were obtained from petrographic studies of selected samples from the Hudson Volcano.

Variation in the magma density (Fig. 4a) strongly depends on the content of exsolved phases, particularly the magnetite and H_2O content. A variation of up to 7% in magma density has been recorded as a result of this effect. The calibration of the liquid density included the thermal and compositional effects. The decrease in temperature accounts for an increase of up to 1% in liquid density, whereas the compositional effects account for a decrease in liquid density of up to 10%. The incompressible character of the magma assumed in our formulation gives rise to an error of 0·3% for the magma density. The calibrated density at 900°C of both magma (liquid and its exsolved phases) and liquid is 2650 and $2250\,kg/m^3$, respectively.

Magma viscosity depends on the solid and gas content, and, to a lesser extent, on temperature (Fig. 4b). For the determination of the effects of suspended solids on magma viscosity, a maximum packing value of 75% with an exponent of −5/2 in the Einstein–Roscoe equation is assumed (see review of values by Pinkerton & Stevenson, 1992; Petford, 2003). For the H_2O gas effect we assume a maximum packing value of 30% with an exponent of 5/2 in the Einstein–Roscoe equation to give to pure bubbles a stronger influence on magma viscosity than that resulting from the same concentration of pure solids (see inset in Fig. 4b). At crystal contents of 30–50 vol. % a rheological

Table 2: Thermal parameters

Symbol	Value	SI unit	Variable	Object	References
$T\ initial$	1200	°C	initial temperature	magma	
$T\ liquidus$	1131	°C	liquidus	magma	
$T\ final$	926	°C	final calibration temperature	magma	
T_r^0	27	°C	surface temperature	host rock	
G_r	0·03	°C/m	initial geothermal gradient	host rock	
k_m^0	1·5	W/m K	thermal conductivity	magma	1
k_{ol}^0	4·58	W/m K	thermal conductivity	olivine	1
k_{mt}^0	6·08	W/m K	thermal conductivity	magnetite	1
k_{fld}^0	2·26	W/m K	thermal conductivity	feldspar	1
k_{cpx}^0	4·68	W/m K	thermal conductivity	clinopyroxene	1
k_{opx}^0	4·44	W/m K	thermal conductivity	orthopyroxene	1
k_{gas}^0	1·76	W/m K	thermal conductivity	H_2O gas	1
k_r^0	2·6	W/m K	thermal conductivity	host rock	2
Cp_{ol}	1144	J/kg K	heat capacity	olivine	3, 4
Cp_{mt}	1155	J/kg K	heat capacity	magnetite	3, 4
Cp_{fld}	1196	J/kg K	heat capacity	feldspar	3, 4
Cp_{cpx}	941	J/kg K	heat capacity	clinopyroxene	3, 4
Cp_{opx}	1500	J/kg K	heat capacity	orthopyroxene	3, 4
Cp_{gas}	3795	J/kg K	heat capacity	H_2O gas	3, 4
Cp_{liq}	1450	J/kg K	heat capacity	liquid	3, 4
Cp_{gas}	10000	J/kg K	heat capacity	H_2O gas	3, 4
Cp_r	1390	J/kg K	heat capacity	host rock	
L_r	1000	m	distance from the chamber	host rock	3, 4
Ea	500000	J/mol	activation energy	magma	3, 4
qL_{ol}	−283000	J/kg	latent heat	olivine	3, 4
qL_{mt}	−801900	J/kg	latent heat	magnetite	3, 4
qL_{fld}	−52000	J/kg	latent heat	feldspar	3, 4
qL_{cpx}	−113000	J/kg	latent heat	clinopyroxene	3, 4
qL_{opx}	−716700	J/kg	latent heat	orthopyroxene	3, 4
qL_{gas}	516000	J/kg	latent heat	H_2O gas	3, 4

1, Clauser & Huenges (1995); 2, Chapman & Furlong (1992); 3, Ghiorso & Sacks (1995); 4, Asimow *et al*. (1998).

barrier to phase segregation is given by the decrease of the Stokes' velocities by $c.\ 10^2$.

The calculated liquid compositions (Fig. 5) have associated errors smaller than 0·1 wt % for each component, but those associated with the magma compositions (solid + liquid) are larger (<1·5 wt % for SiO_2, CaO and Fe* and <0·5 wt % for the other components). The simulation reproduces the differentiation process from basalt to felsic andesite ($c.\ 60$ wt % SiO_2) liquids.

DESCRIPTION OF MODELING RESULTS

The results provided here are a simplification of the extremely complex evolution of a natural basaltic system based on the modeling described above and should be considered as non-unique because any deviation in thermal, physical and compositional parameters from values given in Tables 2–4 will change the numerical results to some degree. Visualization of the model results is provided in video format at the *Journal of Petrology* website (see Supplementary Data).

Magma fluid dynamics: variations of convective movements in the magma chamber

Three liquid convection patterns are identified: cell circulation, thin liquid layer flow, and downward and upward plumes. All of these coexist with variable velocities decreasing with time (Fig. 6b).

Table 3: Physical parameters

Symbol	Value	SI unit	Variable	Object	References
μ^0	1·95	Pa s	initial viscosity	magma	1, 2
n_s	−2·5		viscosity parameter	solid	
n_g	2·5		viscosity parameter	H_2O gas	
ϕ_s	0·75		maximum packing value	solid	
ϕ_g	0·30		maximum packing value	H_2O gas	
ρ_m	2510	kg/m^3	density	magma	1, 2
ρ_{ol}	3305	kg/m^3	density	olivine	1, 2
ρ_{mt}	4484	kg/m^3	density	magnetite	1, 2
ρ_{fld}	2662	kg/m^3	density	feldspar	1, 2
ρ_{cpx}	3283	kg/m^3	density	clinopyroxene	1, 2
ρ_{opx}	3279	kg/m^3	density	orthopyroxene	1, 2
ρ_{gas}	1808	kg/m^3	density	H_2O gas	1, 2
ρ_r	2600	kg/m^3	density	host rock	1, 2
r_{ol}^0	0·010	m	critical radius	olivine	
r_{mt}^0	0·008	m	critical radius	magnetite	
r_{fld}^0	0·005	m	critical radius	feldspar	
r_{cpx}^0	0·008	m	critical radius	clinopyroxene	
r_{opx}^0	0·008	m	critical radius	orthopyroxene	
r_{gas}^0	0·001	m	critical radius	H_2O gas	

Table 4: Compositional parameters obtained from Ghiorso & Sacks (1995) & Asimow et al. (1998)

| Symbol	Value	SI unit	Variable	Object
ϕ_{ol}^f	0·0484		final volume fraction	olivine
ϕ_{mt}^f	0·0377		final volume fraction	magnetite
ϕ_{fld}^f	0·507		final volume fraction	feldspar
ϕ_{cpx}^f	0·1328		final volume fraction	clinopyroxene
ϕ_{opx}^f	0·0353		final volume fraction	orthopyroxene
ϕ_{gas}^f	0·2321		final volume fraction	H_2O gas
T_{ol}^m	1102	°C	mean temperature	olivine
T_{mt}^m	1070	°C	mean temperature	magnetite
T_{fld}^m	1010	°C	mean temperature	feldspar
T_{cpx}^m	1110	°C	mean temperature	clinopyroxene
T_{opx}^m	965	°C	mean temperature	orthopyroxene
T_{gas}^m	980	°C	mean temperature	H_2O gas
σ_{ol}	30		standard deviation of exsolution rate	olivine
σ_{mt}	40		standard deviation of exsolution rate	magnetite
σ_{fld}	50		standard deviation of exsolution rate	feldspar
σ_{cpx}	10		standard deviation of exsolution rate	clinopyroxene
σ_{opx}	20		standard deviation of exsolution rate	orthopyroxene
σ_{gas}	20		standard deviation of exsolution rate	bubble H_2O
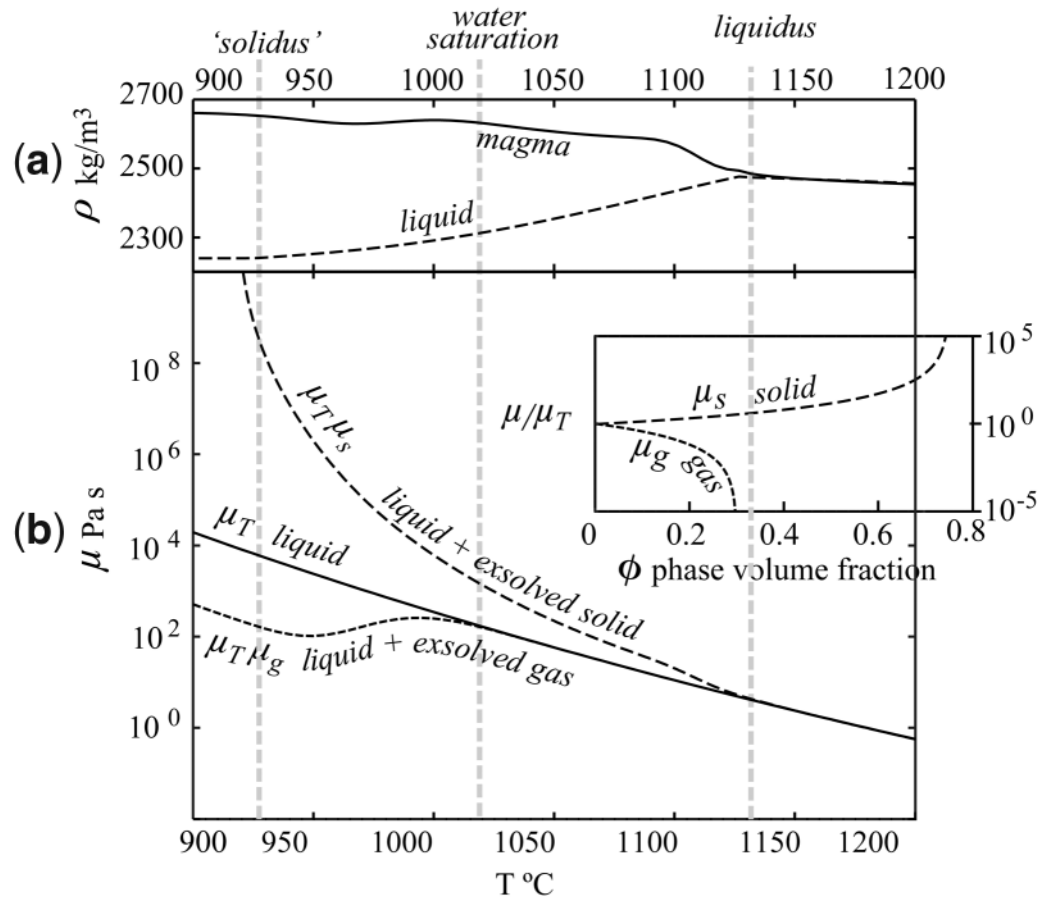
Fig. 4. Variations in the calibrated physical properties of liquid and magma (liquid and its exsolved phases) with temperature, regardless of the position in the chamber: (a) density; (b) viscosity. Liquid density is calibrated from MELTS, including the thermal and compositional effects. Crystallization increases the overall magma density despite the effect of H_2O gas expansion at 1000°C. Liquid viscosity calibrated from MELTS increases following Arrhenian behavior (continuous line). The effect of exsolved solids and gas, considering Einstein–Roscoe behavior, is included (dashed lines). The effect of exsolved phases (solid and gas) on viscosity (see inset) is about 10^5 for 75 vol. % solids and about 10^{-2} for 20 vol. % H_2O gas.

Cell circulation

Cell circulation of liquid takes place in different parts of the chamber during the 10 kyr of cooling. During the first 1.5 kyr large convective cell circulation occupies most of the magma chamber volume. At about 3 kyr, liquid circulation generates two convective cell domains located in the upper and lower half of the chamber, respectively. The upper cell propagates downward, leaving the uppermost part of the chamber nearly stagnant. On the other hand, the lower convective cell is continuously reduced up to the lower third of the chamber and perturbed by ascending plumes from the chamber floor. At the end of the numerical experiments, only the cells in the lower half of the chamber survive.

Plumes

Convection initiates vigorously with the upward and downward displacement of lighter and heavier liquid layers from the bottom and roof, respectively (Fig. 7). Subsequently, vertical plumes start to move as discrete magma pulses, in which the intervals between pulses are controlled by the required time for the buoyancy derived from density contrasts to exceed the viscosity barrier for liquid displacement. Each interval is therefore controlled by the temperature and compositional distribution within the magma chamber. At about 0.4 kyr plumes from the floor start ascending, followed by plumes descending from the roof. Descending plumes within the central part of the chamber reach velocities as high as 40 m/yr at about 0.5 kyr (Fig. 7a). Plumes of differentiated liquid permanently rise from the floor and may reach about 1 km in diameter in vertical section and velocities as high as 30 m/yr at about 3 kyr. They do not significantly affect the upper part of the chamber, where the magma becomes nearly stagnant after a few thousand years (Fig. 7a).
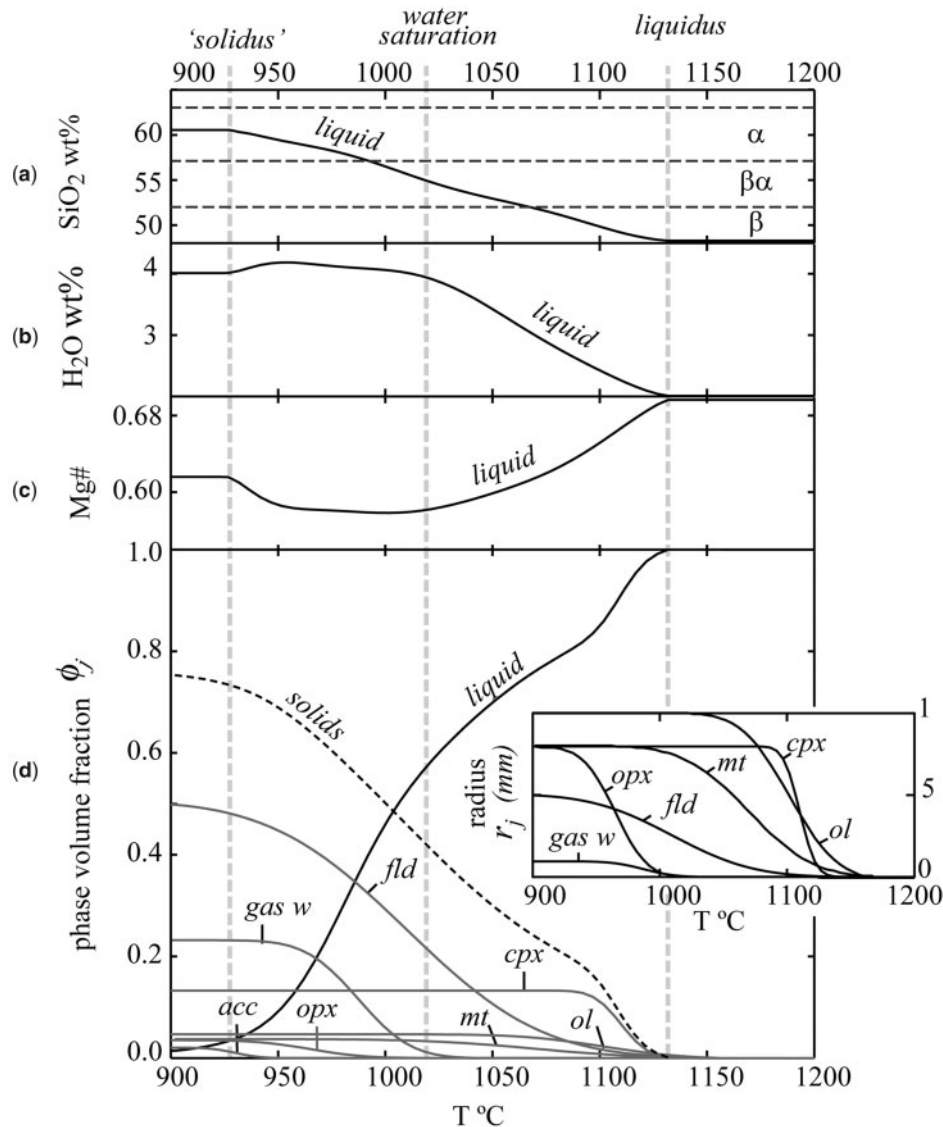
Fig. 5. Variations of compositional parameters with temperature of liquids and phase volume fractions (calibrated from MELTS) and regardless of the position in the chamber: (a) silica content; (b) H_2O content; (c) Mg-number; (d) phase volume fraction. Inset in (d) shows the radii of the exsolved phases with decreasing temperature, used in the model. We reproduce the compositional variation of the liquid during 220°C of undercooling. The compositional evolution from basalt (β) to andesite (α) is obtained by fractional crystallization of olivine (*ol*), clinopyroxene (*cpx*), magnetite (*mt*), and late orthopyroxene (*opx*). H_2O exsolution (*gas w*) takes place in a basaltic andesite liquid (βα) with 4 wt % of H_2O at 1020°C. Late exsolution of accessory minerals (*acc*), including rhombohedral Fe–Ti oxides, produces an increase of Mg-number values at 950°C in the remaining liquid (5 vol. %); fractionation of other accessory phases is neglected because of their low volume content.

Thin layer flows

Because of sucking generated by the vigorous convection of liquid layers on melts near the roof and floor (*c.* 0·3 kyr; Fig. 6b), the initial plumes propagate laterally until the walls or central axis are reached. From there the magma ascends or descends as thin layers that flow at the highest velocities (*c.* 60 m/yr; Fig. 6b). The ascending and descending liquids near the walls coexist during almost the entire 10 kyr, forming thin magma layers that flow with opposite sense (Fig. 7). The upward thin layer flow occurs adjacent to the walls (outer layer flow) as a consequence of liquid density reduction after sidewall differentiation. The downward flow occurs adjacent to the outer layer flow occupying an inner position (inner layer flow) and is generated by thermal contraction upon magma cooling at the roof. During the final stages of the numerical experiments, the magma adjacent to the walls flows at moderate velocities of about 8 m/yr. The high velocities of these layer flows during the early stage of cooling generate relatively high shear rate domains against the wall and between the two
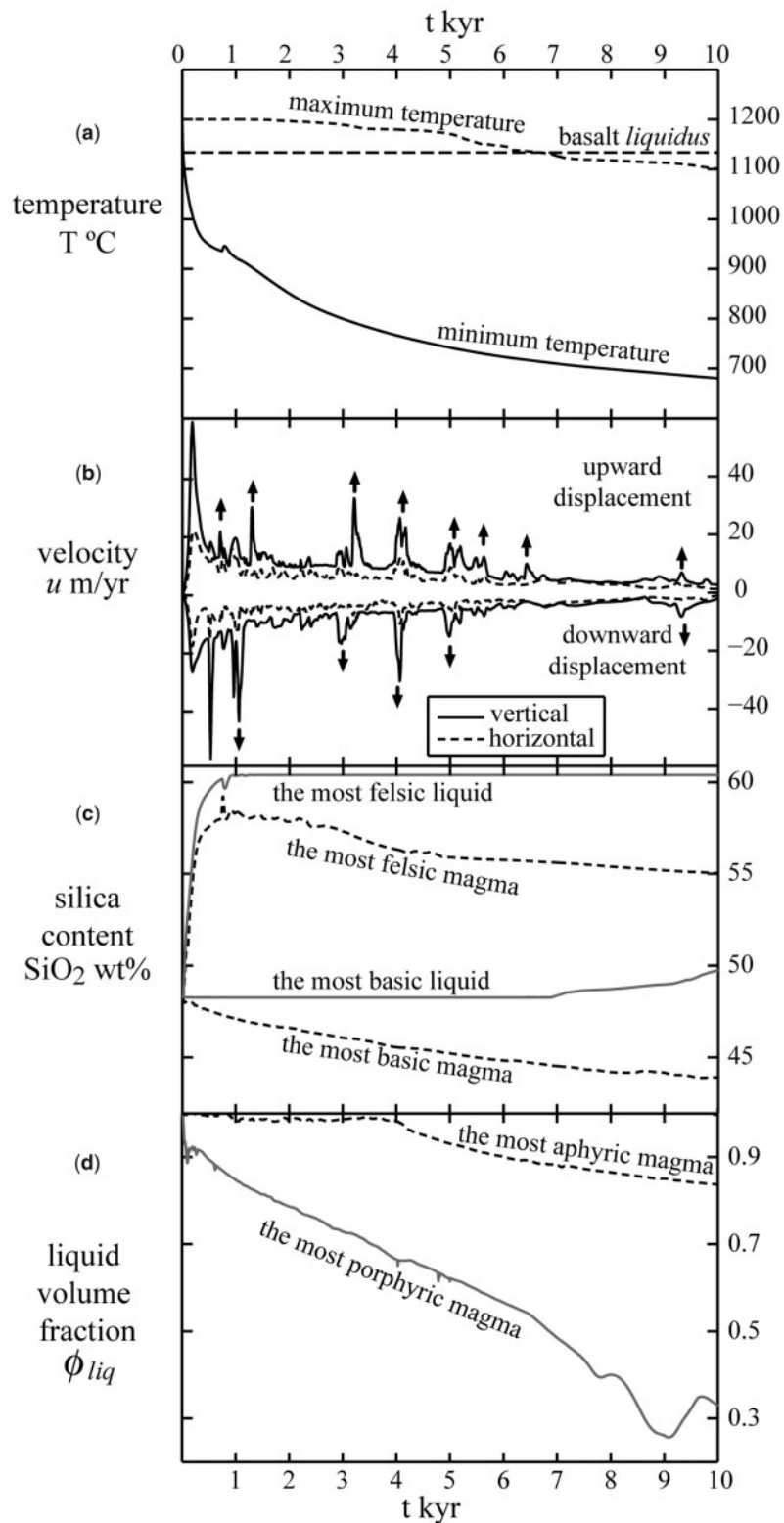
Fig. 6. Extreme values record of physical and compositional parameters of coexisting magmas during the l0 kyr of chamber evolution: (a) temperature; (b) convective velocity; (c) silica content; (d) liquid volume fraction. It should be noted that: (1) a temperature difference as large as 300–400°C between coexisting magmas is recorded since the early stages of cooling; (2) convective velocities in the magma are characterized by time-decreasing peaks, mainly given by magma pulses; the vertical component of magma flow velocity is higher than the horizontal velocity component; (3) a silica-rich (60 wt % SiO$_2$) magma is formed early (<l kyr) in the system; (4) liquid with initial composition remains unmodified up to 7 kyr; (5) aphyric magmas persist up to 4 kyr.
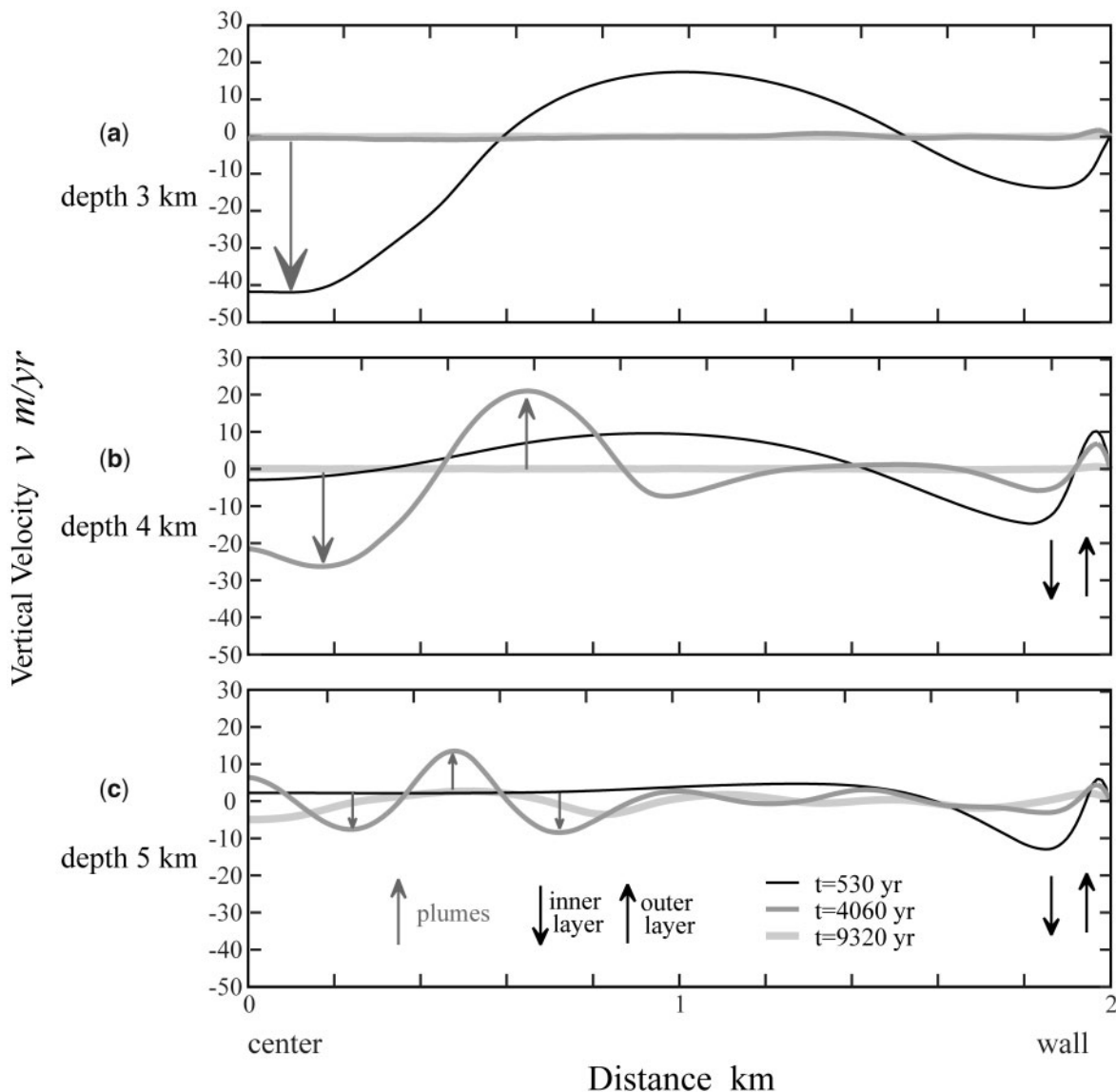
Fig. 7. Profiles from center to wall of the reservoir showing vertical flow velocities of the liquid at selected times. Profiles (a), (b) and (c) correspond to 3, 4 and 5 km depth, respectively. Arrows show the maximum velocity of plumes and inner and outer layer flow for the respective time.

layers. The width of the inner layer flow is variable, between about 300 and 500 m, whereas the width of the outer layer flow is about 50–100 m (Fig. 7). The outer layer flow is the main mechanism by which differentiated magmas accumulate at the top of the chamber by the 'filling-box' mechanism (Fig. 8; Turner & Gustafson, 1981). Because of successive upward flows, the thickness of the stratified column of differentiated magma progressively increases from the top of the chamber. For example, at 10 kyr the upward layer flow feeds the base of the differentiated magma column, located at about 1 km from the floor (Fig. 8f).

Thermal structure of the country rocks

The temperature distribution within the wall-rocks is variable with time, depending on two related factors: the temperature distribution in the chamber interior and the efficiency of heat transfer from the magma. The zones of the chamber exhibiting lower temperatures are restricted to magmas adjacent to the roof and vertical walls during the 10 kyr of simulation. The lowest temperatures are recorded in magma collected in the upper corners of the chamber, where the cooling surface is the largest. The side-wall magma flow partially insulates the chamber from the colder wall-rocks; consequently, heat transfer across
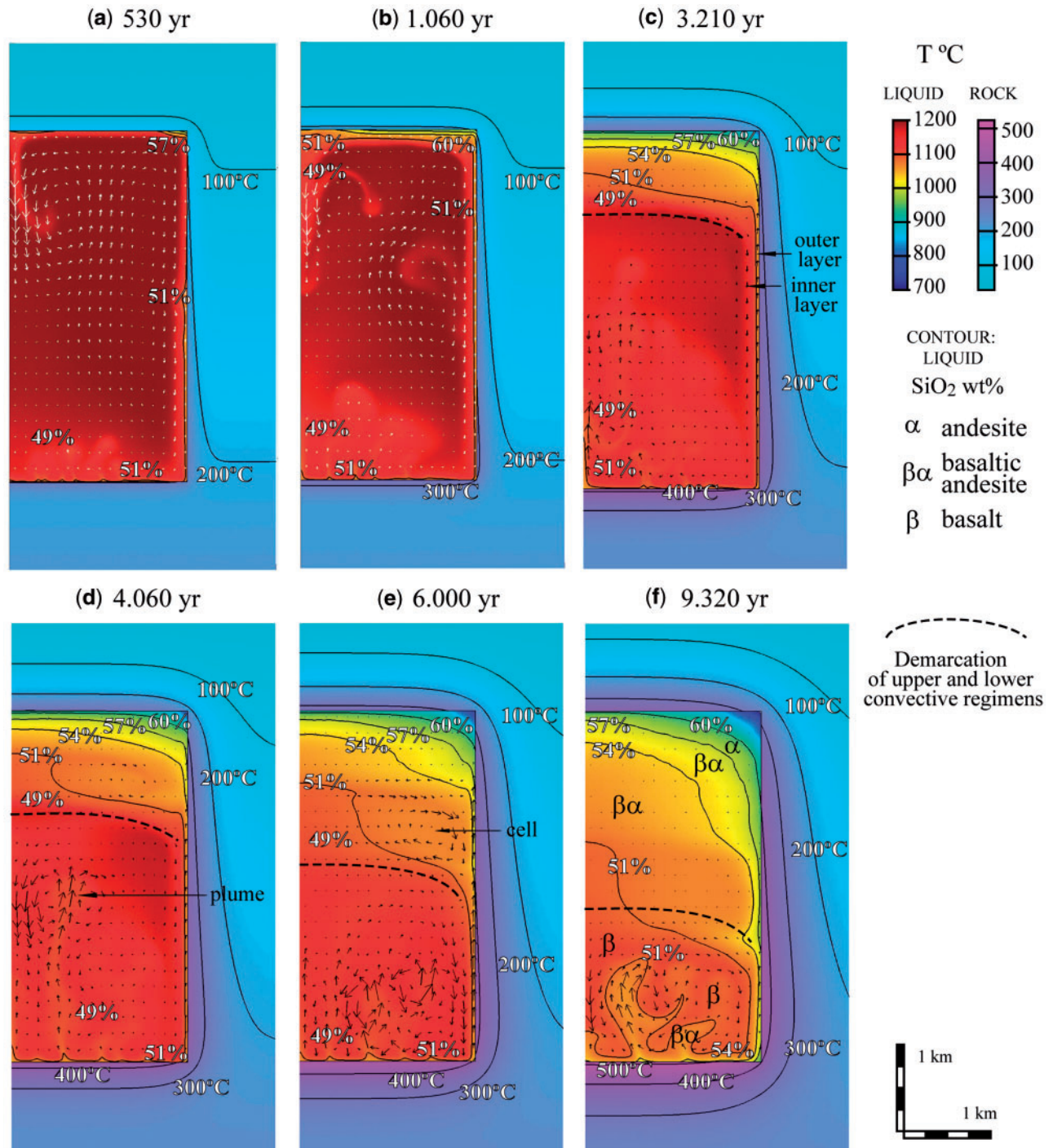
Fig. 8. Images (2D) of the right half of the chamber showing variations in temperature and silica content of the liquid at selected moments when a peak of high-velocity convection occurs (see Fig. 5b). Isotherms in the country rocks show an increase of about 260°C at the floor and 200°C at the roof with respect to the temperature before the intrusion (assuming a thermal gradient of 30°C/km), indicating higher heat flow at the floor than at the roof of the reservoir. Contours indicate the silica content of the liquid. Arrows represent the magma flow velocity vector (normalized at the highest velocity value reached at each selected time) recorded on a regular grid within the chamber. Distinct convective patterns in the magma (plumes, cells and along-wall layer flow) are shown. The upper and lower sections of the chamber develop different convective patterns and a progressive temperature and compositional stratification. It should be noted that the most differentiated liquids concentrate preferentially in the upper corners of the chamber as time proceeds. Residual melts collect in those places where cooling rate and subsequent differentiation are the highest as a result of the influence of wall-rock with the lowest temperature and the largest cooling surfaces (vertical and horizontal) per unit volume.

the vertical walls is less significant than elsewhere across the intrusive contact. Additionally, our simulations indicate that heat loss from the roof of the chamber is less important than commonly assumed, as a consequence of the colder residual liquid collected in the upper levels. The resulting thermal structure of the country rocks is shown in Fig. 8 and is characterized by the highest thermal gradient below the floor of the chamber, where temperatures reach more than $500°C$ after 10 kyr of magma cooling. In other words, the most efficient heat flow is recorded across the floor, as indicated by the highest temperature excess with respect to the temperature prior to the intrusion. For example, the temperature at the depth of the floor before the intrusion is $207°C$ (assuming a thermal gradient of $30°C/km$) and at the roof is $87°C$. At 10 kyr after intrusion the temperature at the floor is $514°C$ (e.g. *c*. 307°C increase), whereas at the roof it is about $378°C$ (e.g. *c*. 291°C increase).

Distribution of the exsolved phases in the magma

Solid phases

The time-dependent distribution of the solid phases inside the chamber obtained from our modeling indicates that crystallization starts from cooling liquids at the floor and walls of the chamber. Crystallization at the floor is also favored by the transference of cooler and denser liquids from the top of the chamber to the bottom. The suspended crystals start concentrating at the lower levels of the chamber, from where they progressively propagate upward, giving rise to a well-defined stratification of upward decreasing concentration of solids. At 10 kyr (Fig. 9b), the volume fraction of solids in the lower half of the chamber varies downward from 35 to 65 vol. %, whereas the solid concentration in the upper half ranges between <10 and 35 vol. % from upper to lower levels. The rate of solid concentration at the bottom is nearly constant at about 12 vol. %/kyr, whereas at the top it is in the 1–2·5 vol. %/kyr range. The spatial distribution of each solid phase (Fig. 9d–h) is controlled by the combination of the suspended solid velocities in the liquid and the convective magma flow velocities. Olivine, magnetite and clinopyroxene accumulate at the floor with an upward-decreasing concentration. For example, after 10 kyr of magma evolution, olivine can reach a concentration of about 8 vol. % adjacent to the floor, but is absent at the roof of the chamber. Clinopyroxene, which is by far the most abundant mafic phase in the chamber, also shows a gradation from about 25 vol. % at the bottom to less than 1 vol. % near the roof of the chamber after the same time span of crystallization. In contrast, the small amount of orthopyroxene formed during the 10 kyr of magma cooling does not

fractionate, and is concentrated in differentiated liquid adjacent to the roof and along the upper walls.

The plagioclase feldspar distribution (Fig. 9g) is strikingly different from the mafic phase distribution. A concentration of about 20 vol. % of plagioclase crystals along the roof and upper walls is achieved at 5 kyr. Further plagioclase crystallization expands downward along the walls and a plagioclase-dominated crystallization front starts forming in the upper corners at about 4 kyr, because of the high viscosity and almost null density variation of the boundary layer. At 10 kyr, concentrations as high as 25–30 vol. % are recorded along the wall and bottom of the chamber, decreasing to less than 10 vol. % in the chamber interior.

Along-wall crystallization front

Crystallization along near-vertical wall-rock contacts has been invoked as an efficient mechanism to generate boundary layers of buoyant residual melt able to migrate upwards and collect at the top of the chamber (see McBirney, 1980; Turner, 1980; Spera *et al.*, 1984; Wolff *et al.* 1990; de Silva & Wolff, 1995; Marsh, 1996). This situation is reproduced in our modeling as a consequence of the steep temperature gradients across the wall-rock contact. Despite the fact that a condition that allows crystals to stick at the walls of the chamber was not imposed in our simulations, a crystallization front along the walls is obtained by retention of an increasing amount of crystals in progressively more viscous magma as temperatures decrease. Our results indicate that the temperature gradient alone is not enough to generate an early crystallization front. The crystallization along the vertical margins does not culminate in a crystallization front until about 4 kyr of the studied crystallization history when the velocity of the circulating magma (and shear stress) along the walls decreases. Plagioclase is by far the most abundant phase that constitutes the crystallization front (Fig. 9g) because it mainly crystallizes from sidewall-differentiated liquids. The along-wall plagioclase crystallization front propagates from the top to bottom of the magma chamber.

Exsolved H_2O

The initial basaltic liquid, with 2 wt % H_2O at $1200°C$, starts to exsolve H_2O after mineral fractionation resulting from about $180°C$ of cooling (Fig. 5b). The exsolution of H_2O bubbles is initiated at 4 wt % and at about 1 kyr when H_2O-enriched differentiated liquids, formed along the walls and at the bottom of the chamber, ascend and collect in the upper corners of the chamber. From the corners, additional exsolved H_2O propagates laterally, occupying the whole of the uppermost levels of the chamber at about 1·5 kyr. H_2O also propagates downward from the roof, giving rise to a noticeable stratification in the exsolved H_2O content. The upward H_2O propagation is more efficiently produced along the walls. The final

(a) liquid **(b)** solid **(c)** gas H$_2$O **(d)** olivine

(e) magnetite **(f)** clinopyroxene **(g)** feldspar **(h)** orthopyroxene
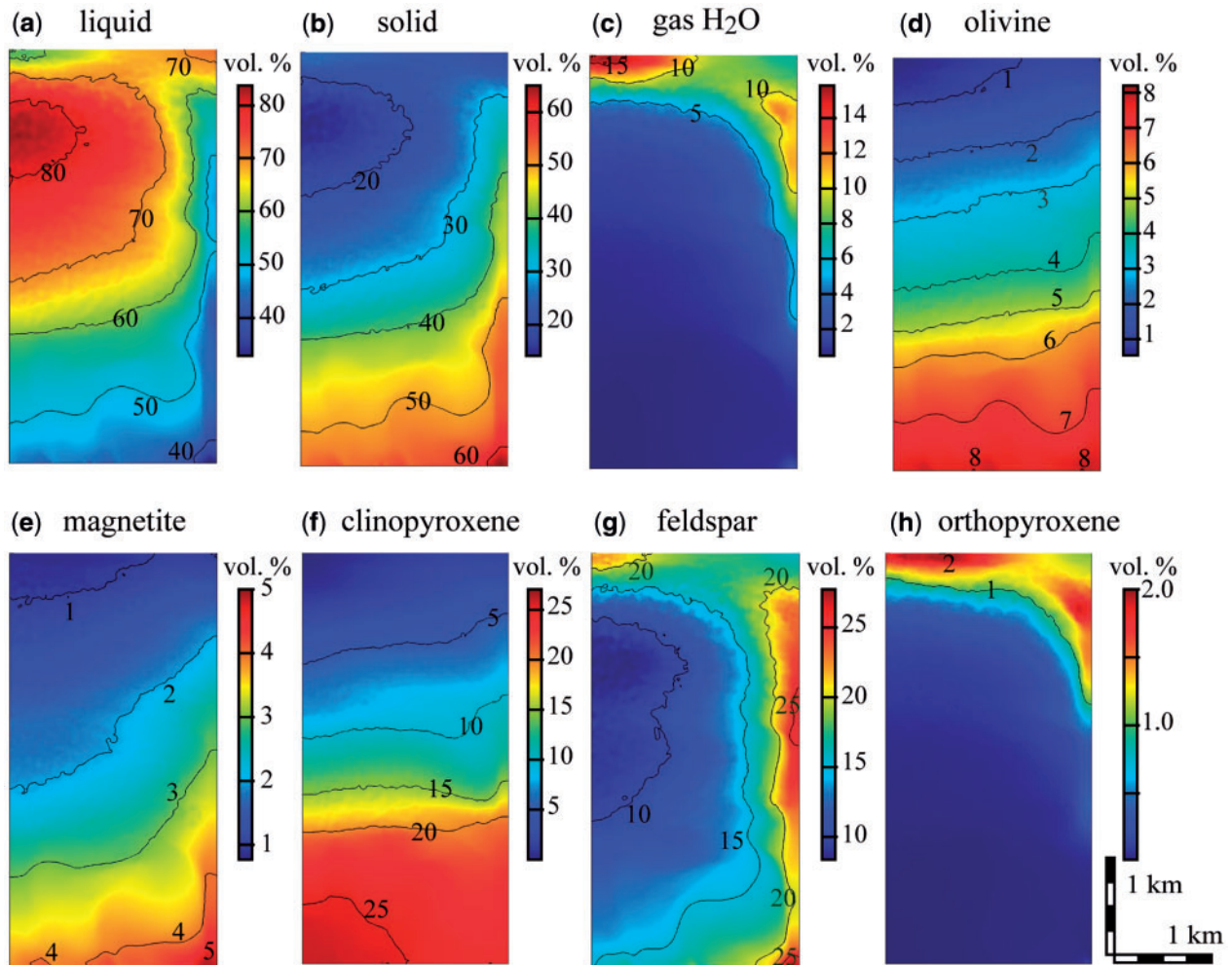
Fig. 9. Images (2D) of the right half of the chamber showing the volume distribution of liquid and exsolved phases at 10 kyr. Residual liquid is concentrated in the upper section of the chamber. Early formed olivine, magnetite and clinopyroxene concentrate at the bottom, whereas late minerals (plagioclase and orthopyroxene) and H$_2$O gas are collected at the roof and vertical walls.

distribution (at 10 kyr) of exsolved H$_2$O is shown in Fig. 9c. The exsolved H$_2$O is more concentrated in H$_2$O-saturated liquids (H$_2$O > 4 wt %) along the central part of the roof and the upper walls, reaching 16 and 12 vol. %, respectively.

Compositional zonation of the chamber: liquids and magmas

Here we describe the time-dependent compositional variations inside the chamber for the liquids and magma (liquid + solid + gas) separately because the magnitudes of the compositional gradients in each case are strikingly different.

Liquids

The modeling provides evidence of coexistence of liquids of different composition inside the chamber at almost any moment during the cooling history. For example, a range

of silica content as high as 52–60 wt % is recorded in coexisting liquids since the early cooling stages (Fig. 8). The H$_2$O content in coexisting liquids within the chamber is highly variable from an initial content of 2 wt % to the H$_2$O saturation limits of the respective liquids (e.g. 4·1 wt % of the initial melt composition).

Cooling of the superheated liquid starts at the margins of the chamber, where a high temperature contrast between the liquid and the colder country rocks exists. The convective motion produced by cooling of the superheated melt at the top and crystallization of the melt at the base of the chamber are the main mechanisms of mass and heat transfer inside the chamber and produce the coexistence, at almost any time, of liquids with compositional differences of about 10 wt % SiO$_2$ (Fig. 6c) and temperature differences of about 300°C. For example, at 6 kyr, liquids with 60% SiO$_2$ and at *c*. 850°C have collected at the top and upper corners of the chamber, whereas

overheated liquid with 48 wt % SiO_2 at about 1150°C is preserved at the bottom (Fig. 8e).

Upward transfer of differentiated and colder liquids gives rise to thermochemical stratification that starts with thin subhorizontal layers at the top of the chamber. Accommodation at the top by density of the continuous flows of differentiated magma gives rise to a well-defined compositional stratification that propagates downward to the middle part of the column at about 9 kyr (Fig. 8f). The rate of differentiated layer growth is about 100–500 m/kyr, which is comparable with the rates indicated by de Silva & Wolff (1995) for chambers with this geometry and similar volume. This stratification consists of layers with thicknesses of the order of tens of meters that increase downward with time. The stratification of the uppermost part of the chamber at 10 kyr is characterized by subhorizontal layers about 50–100 m thick of downward-decreasing silica content and increasing Mg-number and temperature. At the same time, but independently of the along-wall layer flows, plumes ascend from the bottom, giving rise to poorly defined stratification in the lower half of the chamber. Most of the rising plumes tend to dissipate by convective self-mixing with surrounding magma in the lower half. The resulting stratification is clearly distinguished from the overlying stratified magma column by its comparatively thicker (hundreds of meters) and less defined layers, which exhibit a subtle downward decrease in silica and increase in Mg-number. The upper and lower sections of the chamber have independent convective patterns.

Magmas

The spatial distribution of the magma (liquid + solid + gas) compositions at about 9 kyr is given by a marked vertical gradient from andesite at the top to ultrabasic magma at the bottom of the chamber (Fig. 10a). Although a simultaneous strong gradient in silica content is detected in the liquid composition, a comparison between the compositional parameters (silica content and Mg-number) of magmas and liquids shows substantial differences. The most differentiated magma, collected at the top of the chamber, has a lower silica content (about 55 wt %; Fig. 10a) than its liquid counterpart (about 61 wt %; Fig. 8). On the other hand, the magma at the bottom reaches an ultrabasic composition (*c.* 45 wt % SiO_2; Fig. 10a), which is substantially lower than that of the respective liquid. The magma and liquid also show differences in Mg-number gradients, but they are more pronounced in the former. For example, at 10 kyr the range in Mg-number observed in the magmas is as high as 0·62–0·78 but in the liquids is about 0·58–0·65. These compositional deviations between the magma and liquid compositions highlight the significant role of solid phases in the composition of the magmas. Accordingly, most of the suspended crystals did not form in equilibrium with the

hosting liquid, because they were fractionated in variable proportions (i.e. selective fractionation of Cox & Mitchell, 1988). On the contrary, in most cases they may represent antecrysts, following the W. Hildreth terminology (Penrose Conference, 2001; see Hildreth & Wilson, 2007; Putirka, 2008; Cooper & Reid, 2008); that is, crystals inherited from elsewhere in the chamber.

To determine the magnitude of the dispersion of the solid phases suspended in the liquid, a dispersion parameter of the solid phase $D\phi$ (vol. %) within the magma chamber is defined here as

$$D\phi = 100(\phi^e - \phi^d) \qquad (27)$$

where ϕ^e is the solid fraction suspended in the liquid (solidosity; e.g. Petford, 2003) and ϕ^d is the total fraction of exsolved solid phases necessary to form the same liquid. Thus, $D\phi > 0$ indicates that the excess of crystals (in volume fraction) formed elsewhere in the chamber, but concentrated in the particular magma domain, and $D\phi < 0$ indicates depletion in the solid fraction with respect to that necessary to form the liquid. $D\phi = 0$ is not an indication of crystal–liquid equilibrium because the existing solids could be formed earlier and/or from different liquids of the chamber. It is interesting to note the progressive increase in $D\phi$ (i.e. fraction of accumulated crystals) in the magmas with increasing depth in the chamber, reaching +40 at 8 kyr, whereas the opposite occurs with the differentiated magmas at the top of the chamber, where progressive depletion in suspended crystals towards the top of the chamber is recognized. Crystal depletion is also observed in magmas along the walls with respect to the adjacent interior magmas. Such depletion indicates that crystals formed at the walls are dispersed back into the main magma volume (Fig. 10b). Liquids with $D\phi$ of about −60 in the first 3 kyr are restricted to the uppermost levels (contour Fig. 10b), but afterwards liquids exhibiting negative $D\phi$ values propagate downward. Most of the fractionated phases yielding the more differentiated magmas were retained in and/or incorporated into the magma of the lower part within the chamber.

Application of the model to a sill-like magma reservoir

Results

Previous studies based on analogue experiments and numerical modeling, as well as our numerical results, indicate that sidewall fractionation is more efficient than crystal settling as a differentiation mechanism (e.g. Huppert *et al.*, 1986; de Silva & Wolff, 1995). Thus one of the interesting problems in the evolution of magma chambers is the effect of the geometry of the reservoir (i.e. the cooling surface area per unit volume) on the magma fluid dynamics and internal compositional gradients. We selected a cylindrical chamber with an aspect ratio of 0·125 (see
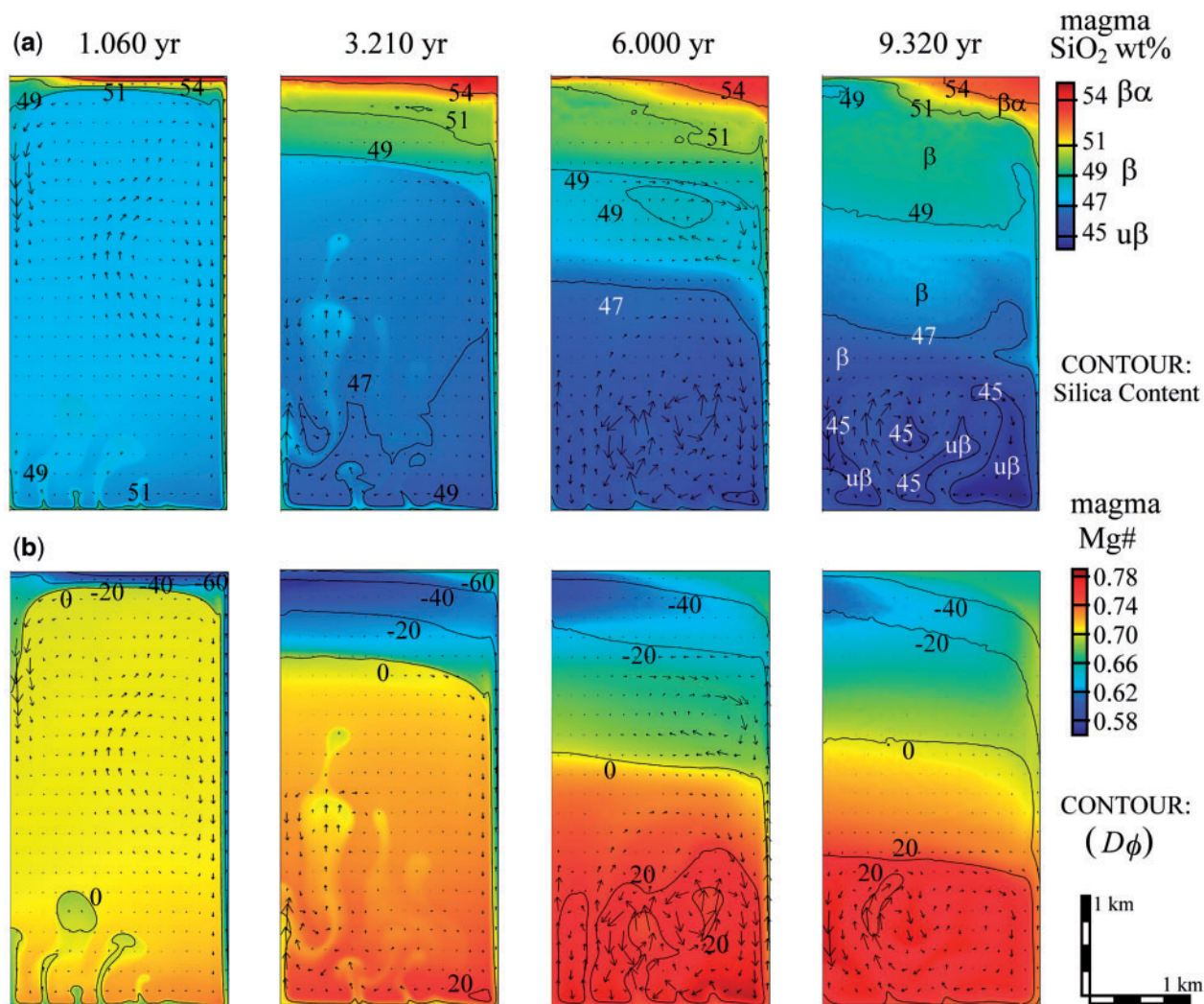
Fig. 10. Images (2D) of the right half of the chamber showing silica content (a) and Mg-number (b) of the magma at the same times as in Fig. 8. The tendency towards ultrabasic composition (c. 45 wt % SiO$_2$ and Mg-number c, 0·8 at 10 kyr) of the lower half-chamber with time, caused by olivine, clinopyroxene and magnetite accumulation, should be noted. Contours in (b) indicate the values of the solid dispersion parameter ($D\phi$; see text for explanation) where positive and negative values of a particular domain of the reservoir indicate enrichment and depletion of suspended solid content (vol. %) in the liquid with respect to the volume of minerals that was exsolved from that liquid. Arrows represent the velocity vector of the liquid as explained in Fig. 8 caption.

Appendix C for details on the geometry) to simulate 10 kyr of cooling of a basaltic sill intrusion emplaced at shallow depth (4 km for the central horizontal axis). Unlike a stock-like body, a sill-like magma chamber has a larger cooling surface area per unit volume and shorter vertical walls, which exert an influence on the time-dependent magma dynamics and compositional variations that can be derived from the numerical simulation. The basis and governing equations, initial conditions and parameter calibration for the experiments are identical to those used for the stock-like chamber. The thermal effect of heat flow from the chamber is also considered. A summary description of the magma dynamics and thermo-compositional

zonation in space and time during 10 kyr of magma chamber evolution is given below.

Rapid cooling of 250°C is recorded in the residual liquid during the first 1 kyr (Fig. 11a). After 0·5 kyr of cooling, a differentiated magma layer ascends along the vertical walls up to the roof, where interaction with hotter liquids takes place. Descending and ascending plumes from the roof and floor, respectively, initiate at about 1 kyr, transferring colder and denser magma to lower levels and residual and lighter magma to the upper part of the chamber (Fig. 12a). At 5 kyr plumes from the roof no longer descend, whereas ascending plumes from the floor are preserved up to the end of the 10 kyr simulation (Fig. 12c). Convection
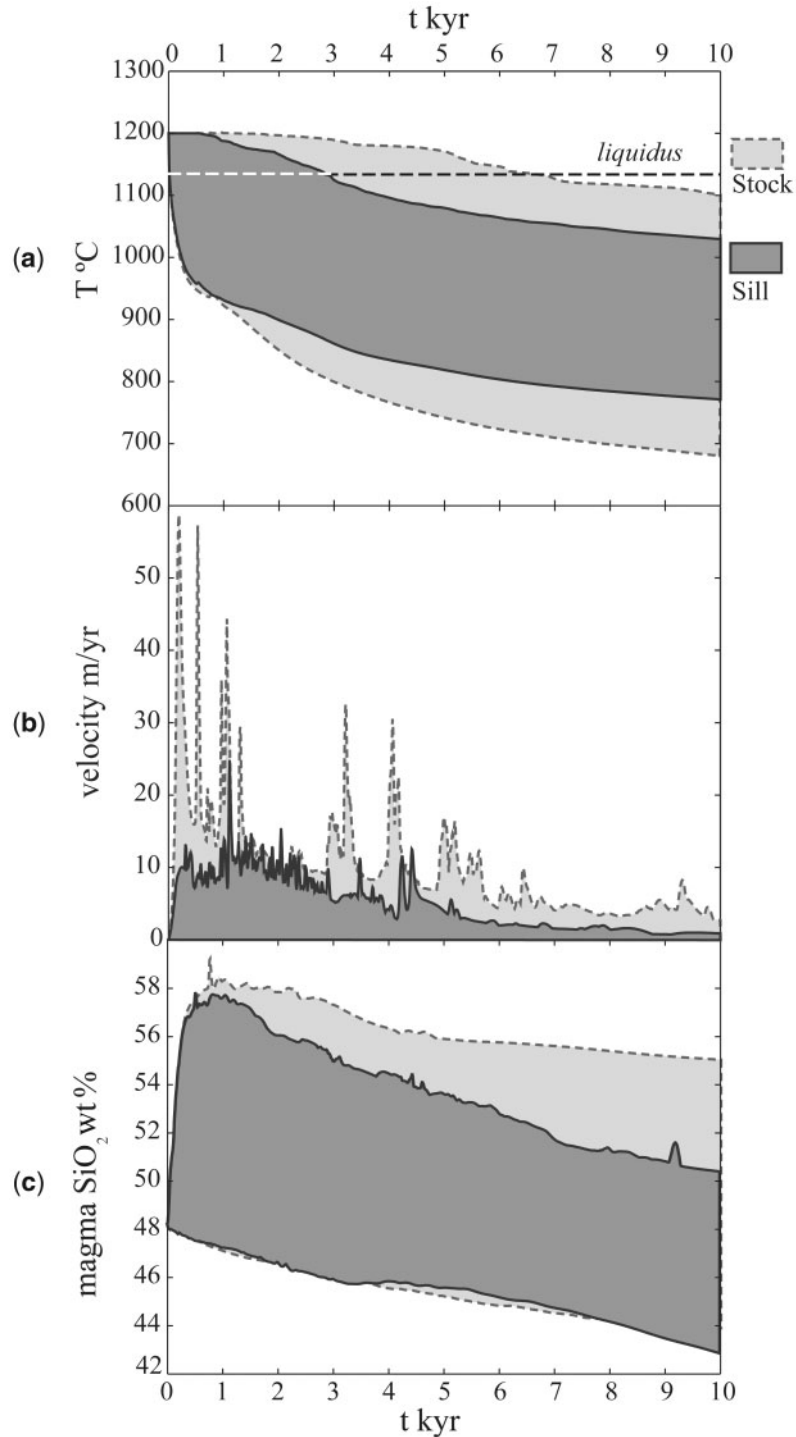
Fig. 11. Extreme values record of physical and compositional parameters of coexisting magmas during the l0 kyr of chamber evolution of the sill-like reservoir (dark grey) and stock-like reservoir (light grey): (a) temperature; (b) velocity; (c) magma silica content. The comparison indicates that the sill-like chamber (low aspect ratios) exhibits (1) lower flow velocities but higher frequency of magma pulses than the stock-like chamber, and (2) smaller range of temperature and silica content of the magma with time than the stock-like reservoir. The more homogeneous distribution of temperature and composition in the sill reflects less efficient sidewall differentiation as a result of the shorter vertical wall, among other factors.
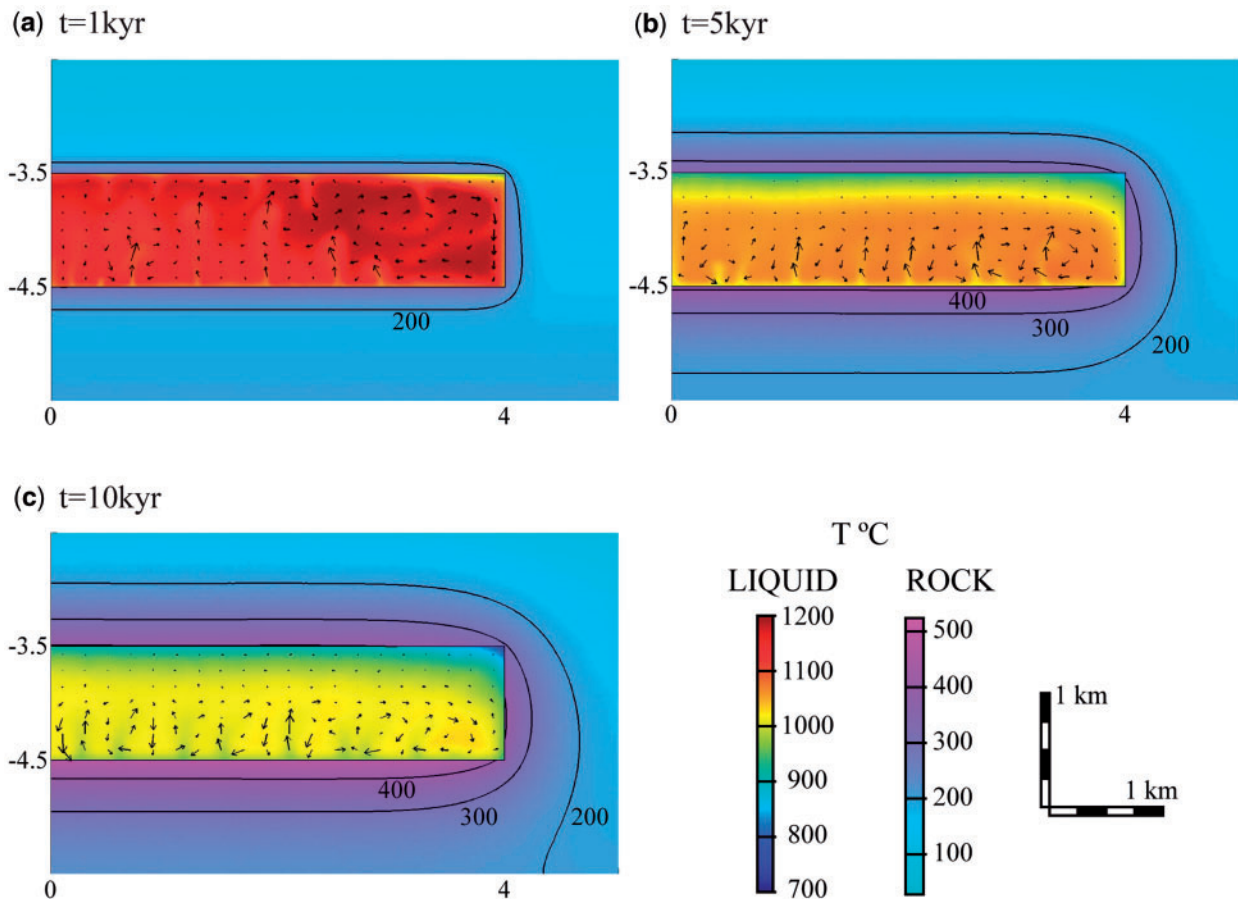
Fig. 12. Images (2D) of the right half of the sill-like chamber showing variations in temperature and silica content of the liquid at 1 kyr (a), 5 kyr (b) and 10 kyr (c). For comparison, temperature color scales are the same as in Fig. 8.

velocities progressively decrease with time (Fig. 11b). During the first 5 kyr plumes and magma convection along the walls ascend or descend at velocities as high as 25 m/yr. After this, the convection velocities are lower than 5 m/yr.

Thermochemical stratification starts developing in the upper corners of the reservoir as a consequence of the along-wall upward transfer of residual magma from the earliest stages of cooling. At the end of the simulation, well-defined thermochemical stratification is generated in the reservoir (Fig. 13a). In fact, in the uppermost levels of the chamber, a downward-decreasing SiO_2 content and an increasing temperature are noted, from liquid with 60 wt % SiO_2 and 900°C to liquid with 57 wt % SiO_2 and 1000°C. The lowest levels are occupied by residual liquids (900–1000°C and 57–59 wt % SiO_2) that are continuously generated *in situ*. The main magma body in the interior of the chamber has a more homogeneous composition of about 55 wt % SiO_2 and a temperature of 1000°C.

After a period of 10 kyr of crystallization, the solid phases occupy more than 60 vol. % of the magma adjacent to the walls (solidification front) and in the lower corners of the chamber (Fig. 13b). The roof concentrates between 40 and 50 vol. % of the solid. Exsolved H_2O concentrates up to 14 vol. % along the vertical walls and beneath the central part of the roof (Fig. 13c).

A brief comparison with the stock-like magma chamber

A sill-like chamber exhibits comparatively weaker convective dynamics with a maximum flow velocity of about 25 m/kyr compared with the 60 m/kyr of the stock-like reservoir. However, the convective dynamics in the sill-like reservoir gives rise to a frequency of 10 magma pulses/kyr, which is substantially higher than the 4 pulses/kyr in the stock-like chamber and is a consequence of the larger roof and floor surface areas in the former geometry.

Low aspect ratios contribute to a more homogeneous distribution of the magma composition, temperature and exsolved phases within the chamber. For example, vertical compositional gradients are gentler in the sill-like body; the range of about 43–50 wt % SiO_2 obtained after 10 kyr of cooling is narrower than the 44–55 wt % SiO_2 recorded
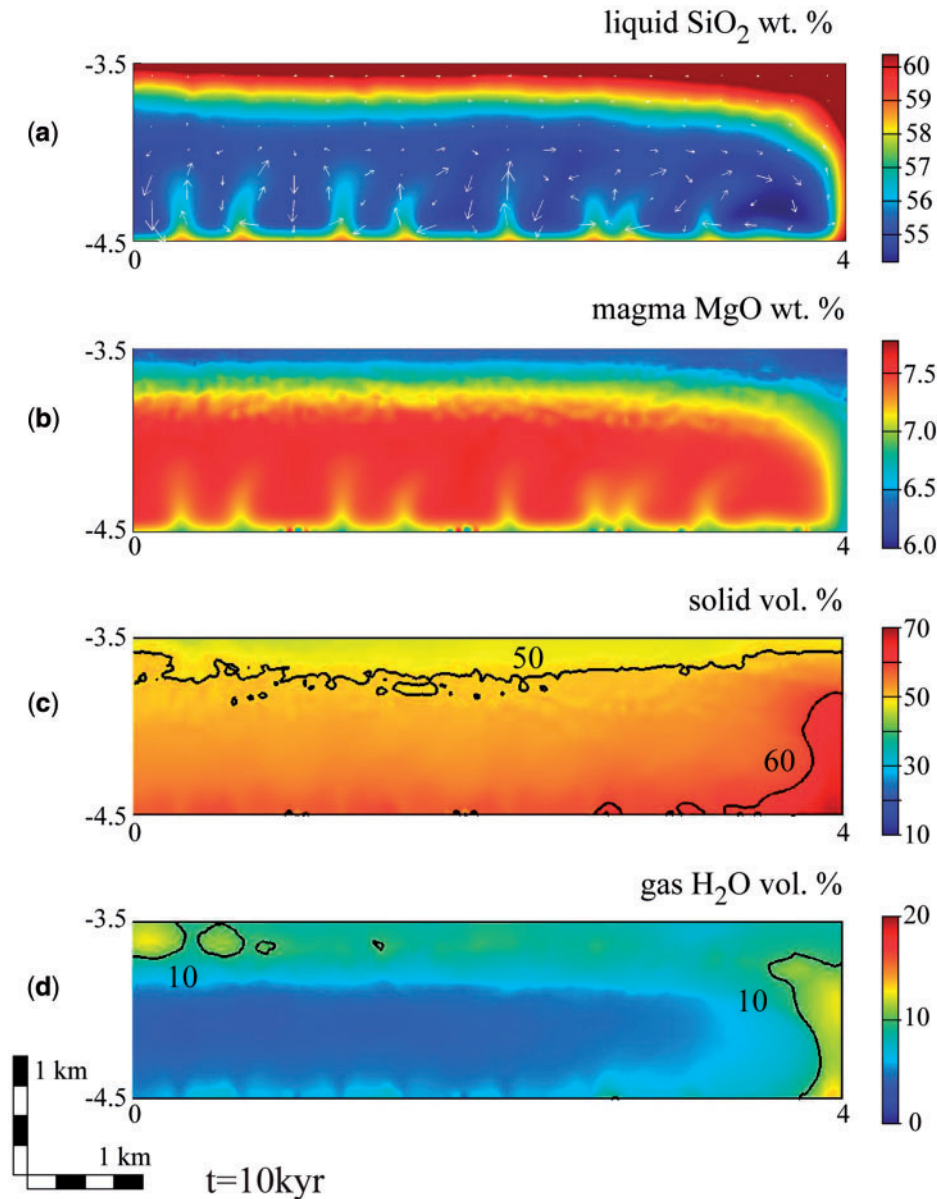
Fig. 13. Images (2D) of the right half of the chamber showing silica content of the liquid (a), magma MgO content (b), solid content (c) and H_2O gas content of the magma (d) at 10 kyr. Arrows in (a) represent the velocity vector of the liquid as explained in Fig. 8 caption. It should be noted that in (a) the upward color diffusion in the ascending plumes from the floor reflects convective self-mixing between residual liquid (c. 60 wt % SiO_2) generated in the floor and the main volume of melt (c. 55 wt % SiO_2).

in the stock-like chamber (Fig. 11c). Simulation of the sill-like reservoir also shows a narrower temperature range (760–1020°C) than that of the stock-like reservoir (680–1100°C) at the end of the 10 kyr. As can be seen from Fig. 11a, superheated melt in the sill simulation is preserved for an interval of about 3 kyr, whereas in the stock-like body it is preserved until about 7 kyr. Exsolved solids and gas concentrate preferentially along the vertical walls and beneath the roof. The volume concentration of

crystals reaches values as high as 60% along the walls at 10 kyr. This concentration is restricted to the lower corners of the stock-like chamber after the same time interval. At the end of the 10 kyr simulation, the solid particle concentration near the roof is as high as 50 vol. %, which is significantly higher than the 20–30 vol. % recorded in the upper levels of the stock-like body, whereas bubble concentration along the roof of the sill body is more diluted than along the roof of the stock.

SUMMARY AND DISCUSSION

From the numerical modeling presented here, a variety of magmatic processes (e.g. convection, crystallization, liquid fractionation, crystal dispersion, magma mixing, volatile transfer) and their compositional effects can be simulated and quantified at any moment and place within two cylindrical basaltic chambers with different aspect ratios (stock-like and sill-like chamber). In the following paragraphs we summarize the main petrological results derived from the model, and their implications for the magmatic evolution of natural closed systems.

Magma fluid dynamics

The fluid dynamics of the early stage convecting basaltic magma chamber are directly related to: (1) cooling of the melt at the roof before the onset of crystallization, as was suggested by Brandeis & Jaupart (1986), giving rise to thermal boundary layers with negative buoyancy allowing the generation of descending thermal plumes, and (2) cooling and crystallization at the floor and along the walls that generate thermochemical boundary layers of buoyant residual liquids flowing upward as plumes and as thin layers along the walls. The thermal effect is provided by two opposite mechanisms: heat transfer from the cooling melt to the host rocks, which are progressively heated, and latent heat released during crystallization. The thermochemical effect is provided by the density of the fluid components removed by crystallization upon cooling (Sparks *et al.*, 1984; Huppert & Sparks, 1984).

Our simulations indicate that convection survived far below the liquidus temperature and continued throughout the whole time span of our experiments, although at moderate velocities. The thermal isolation of the chamber from the colder host rocks provided by the outer and inner layer flows is apparently more significant than other isolation effects (e.g. the isolation effect of the along-wall solidification front). This thermal isolation allows, *inter alia*, the coexistence of superheated initial melts with differentiated basaltic andesite liquids during the first 7 kyr of cooling (Fig. 6a). Compared with the early stages, the velocity of the magma flow is about four times lower during the late stages of chamber evolution. Because our model corresponds to a closed magma system where convection is ultimately generated by cooling through the margins, the convection takes place at rates that are one order of magnitude lower than those estimated for a body of magma heated from an influx of hot magma (Couch *et al.*, 2001).

Viscosity variations as a result of the variable phenocryst content do not stop liquid convection even in a phenocryst-rich melt, implying that the convective liquidus, defined as the temperature below which convection is almost non-existent (see Brandeis & Marsh, 1989), is substantially lower than the true liquidus. Because the

compositional effect on liquid density is about 10 times larger than the thermal effect, crystallization at the floor and along the margins generates the decrease in density necessary for an efficient upward transfer of differentiated liquids. Unlike the upward flow along the walls, which may reach the uppermost levels, the rising plumes from the bottom are mainly restricted to the lower half of the chamber.

The fate of exsolved phases

Because the concentration of phenocrysts and volatiles is highly variable in time and space, it is necessary to evaluate carefully the rheological and petrological implications that can be drawn from the exsolved phases in the simulated cooling chambers. Some of these implications are discussed below.

A tendency for mafic phenocrysts to migrate downward and concentrate in the lower levels of the chamber, regardless of the host liquid viscosity (i.e. liquid composition), is recognized despite the commonly accepted notion that the volume of suspended crystals increases with increasing melt viscosity (see Hawkesworth *et al.*, 2000). The simulations indicate that the phenocryst content (solidosity) decreases upward from the bottom of the chamber (Fig. 14). In this scenario aphyric and crystal-poor magmas survive in the upper levels of the chamber and during the earlier stages of crystallization. For example, the simulation shows that the concentration of suspended crystals near the roof is less than 0·5 vol. % during the first 4 kyr. This concentration increases to *c.* 30 vol. % at 10 kyr (Fig. 14a). At the same time the concentration of solids in the lower half of the chamber and along the lower vertical walls can be as high as 60 vol. % (Fig. 14d). This solid phase distribution generates contrasting effective viscosities in the lower and upper parts of the chamber. Despite the high effective viscosity that could be reached by the magma in the lower part of the chamber, differentiated interstitial melts are able to move upwards through the crystal mush leaving behind crystal cumulates. In natural systems liquid percolation is probably enhanced by crystal compaction (see Bachman & Berganz, 2004). Although processes of liquid percolation–crystal compaction (Darcy's Law; Spera *et al.*, 1995) were not included in this study, flow differentiation is implicitly considered by the simultaneous magma ascent and gravitational settling of crystals.

The high concentration of crystals in the lower half of the chamber could represent a rigid barrier to evacuation during eruptions of magma accumulated deep in the chamber. For example, 7 kyr of crystallization are enough to exceed the liquid–crystal mush transition and create a rigid crust ($\phi_s > 0·5$–$0·55$; Fig. 6d; Marsh, 1996) of accumulated crystals at the bottom of the chamber. The presence of a rigid barrier at the bottom is also consistent with field and geochronological evidence from many plutons,
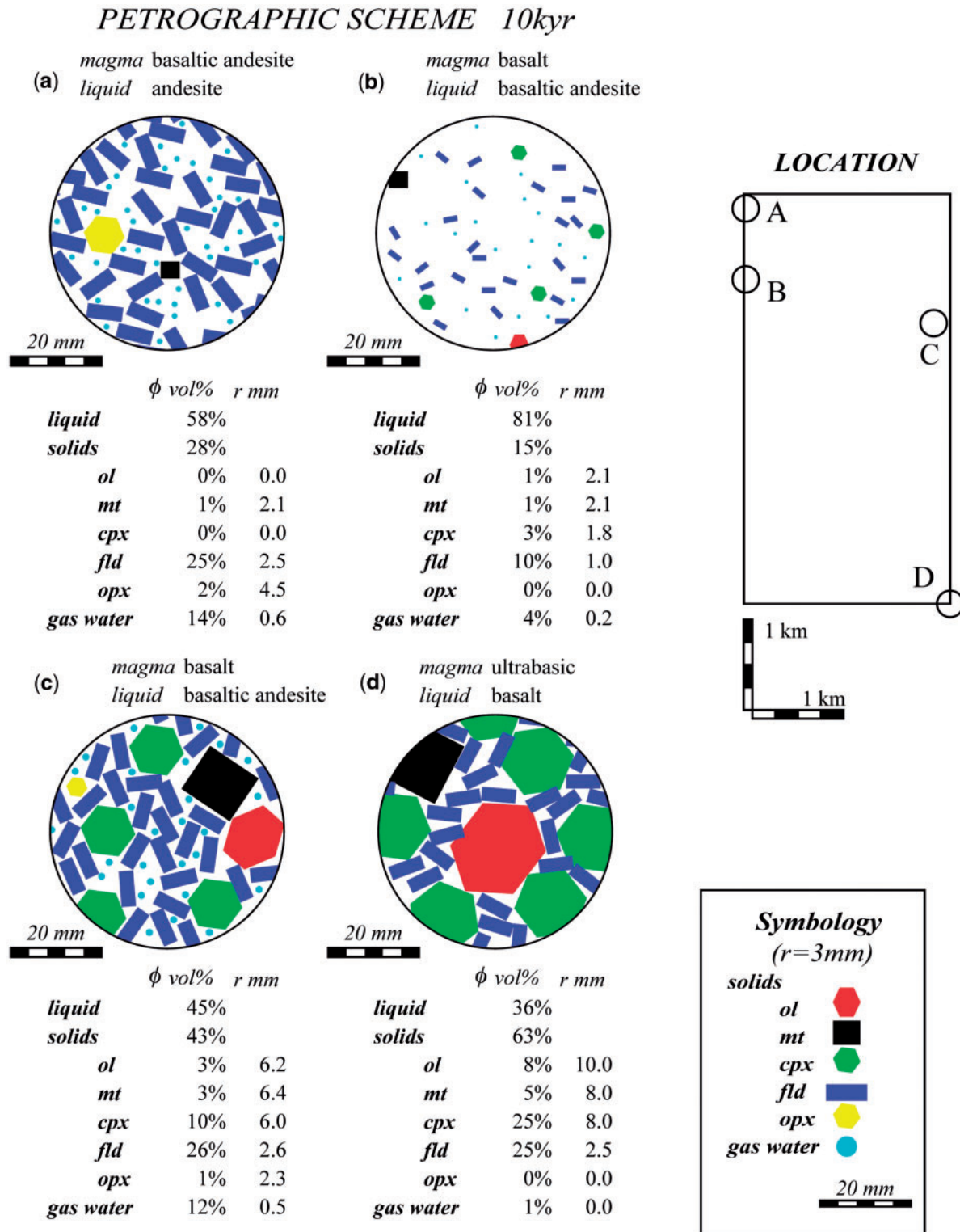
Fig. 14. Modal mineralogy and schematic representation of the textural characteristics of magmas 'virtually' collected at different localities in the chamber after l0 kyr of crystallization.

which indicates that they were formed by the amalgamation of small co-genetic intrusions (Pitcher, 1978; Coleman *et al.*, 2004; Glazner *et al.*, 2004; Matzel *et al.*, 2006), instead of successive events of magma chamber inflation. Finally, the resulting mafic mineral cumulates in typical arc basaltic chambers could generate significant volumes of ultramafic rocks that may trigger gravitationally driven vertical mass transfer, as was noted by Glazner (1994).

A direct genetic link between phenocrysts and the surrounding melt has been commonly accepted; however, the simulations suggest that this assumption may be valid only in exceptional cases. For example, the residual liquids collected in the upper half of the chamber contain lower proportions of solids than the fractionation degree required to generate them. Most of the suspended crystals of plagioclase in these residual liquids could also be formed elsewhere in the chamber (antecrysts). The opposite situation occurs in the lower half of the chamber, where Fe–Ti oxides and ferromagnesian minerals settle. Accordingly, most of the mineral crystals are not in chemical equilibrium with their host liquid. This situation may explain why (1) most plagioclase-rich porphyritic rocks show evidence of plagioclase fractionation (e.g. negative Eu anomalies) and (2) most of the plagioclase and mafic phenocrysts in basic to intermediate lavas exhibit disequilibrium textures, which have been commonly attributed to decompression and/or magma refilling (see Nelson & Montana, 1992). Several studies have indicated that crystals exhibiting disequilibrium features may also form by convective self-mixing (Couch *et al.*, 2001) or by thermal rejuvenation (Bachmann & Bergantz, 2004, 2006; Wiebe *et al.*, 2004) triggered by injection of hotter magma at the base of the chamber. Our results suggest that it is also possible to generate such textures in a closed magma chamber by self-mixing between crystal-laden plumes and the surrounding magma.

If crystal–liquid disequilibrium is the rule, then the temperature and pressure estimates based on phenocryst pairs and phenocryst–groundmass geothermometers and geobarometers should be approached with caution.

A combined solution whereby both gravitational crystal settling and the formation of solidification fronts are operative for segregating crystals from residual liquids is suggested by the numerical simulations presented here, but they do not always occur at the same time. Although along-margin crystallization appears to be a permanent feature during the magma chamber evolution, it does not generate a crystallization front, except during the late stages of the 10 kyr crystallization interval when silicate crystals can adhere along the vertical walls as a consequence of diminishing velocities and increasing viscosities of the liquid layer flow, as well as the low contrast between the liquid and crystal densities. Plagioclase is by far the

most abundant late crystallizing phase and exhibits the lowest density contrast with respect to the surrounding melts. These two aspects imply that plagioclase has the lowest capacity to segregate from a magma with a high effective viscosity. A significant concentration of plagioclase along the walls at the end of the simulation time (Fig. 9g) could reflect the late formation of a vertical crystallization front in the simulated basaltic chamber. The 10 kyr simulations also indicate that a solidification front is not formed at the roof of the stock-like chamber as has been previously suggested (e.g. Marsh, 1996; Christiansen, 2005). However, the simulations of a sill-shaped chamber suggest the formation of a solidification front near the roof, where the crystal concentration is as high as 50 vol. % (Fig. 13b) at 10 kyr.

During the simulated 10 kyr of magma evolution, exsolved H_2O concentrates in the upper levels of the chamber, particularly in residual melts around the central axis (Fig. 9c) where the volume of exsolved H_2O is up to 14% (Fig. 14a). This value can be considered as a minimum because our modeling does not consider the effect of decompression of the rising plumes (equivalent to 4 km of magma chamber height) on magma degassing (Lowenstern, 1994). Because these H_2O-saturated melts have suspended phenocrysts, the resulting magma composition could be as basic as basalt. This situation may explain the explosivity that accompanies many basaltic eruptions, generating in some cases pyroclastic flows (e.g. Williams, 1983; Macleod & Sherrod, 1988; Miyabuchi *et al.*, 2006; Lohmar *et al.*, 2007).

Compositional gradients

Two vertical compositional domains generated by independent convective patterns are identified in the closed stock-like magma system: an upper domain characterized by a well-defined and steep compositional gradient (stratification), and a lower domain exhibiting a less pronounced compositional gradient.

The volume of each compositional layer generated in the upper domain is of the order of 2 km^3, which is similar to the volumes of the erupted materials in a single event. This situation could explain why basic eruptive products are rather homogeneous in composition (e.g. Miyabuchi *et al.*, 2006), despite the compositional variations that are recorded by considering all the eruptive products of a volcanic center. It is worth noting that the total volume percentage of residual felsic melts (*c.* 10% at 10 kyr) is lower than that obtained experimentally from basaltic sources (Sisson *et al.*, 2005). The compositional gradients within the lower domain of the chamber are partially destabilized by advection of differentiated plumes that intermittently rise from the bottom and mix with the surrounding magma. However, a certain volume of the initial liquid

not undergoing fractionation is preserved in this lower domain for a long time.

Because the solid phases suspended in the liquid may have an important effect on the magma (liquid + solids + gas) composition (Fig. 10), which may differ substantially from the liquid composition, caution should be exercised when establishing the compositional evolution of porphyritic igneous bodies.

Compositional gradients generated in the sill-like chamber simulation can be roughly compared with some natural examples. Basic–ultrabasic sills have been identified on the basis of the shape of the modal mineralogical variation or MgO and SiO_2 compositional profile (S-, D- or I-shaped) as a function of stratigraphic height (e.g. Gibb & Henderson, 1992; Marsh, 1996; Latypov, 2003b). These shapes have been interpreted as a result of multiple intrusion (Gibb & Henderson, 1992, 2006) or by *in situ* crystallization of a closed system generated from a single input of crystal-poor parental magma (Latypov, 2003a). The profiles obtained in the current simulations (Fig. 13a and b) are comparable with those of D-shaped sills (e.g. Saline No. 1 sill, Kilmuir sill and Lugar sill; Gibb & Henderson, 1992; Latypov, 2003a), although chilled margins are not reproduced.

CONCLUSIONS

The time–space numerical modeling presented here allows simulation of the cooling and crystallization of a convective chamber and quantifies variations in its temperature, density, viscosity, vector velocities and composition, as well as the distribution of the exsolved phases. Additionally, the model considers the thermal perturbation of the host rocks and its influence on the cooling pattern of the chamber. The simulation of a closed stock-like body results in a compositionally stratified chamber, involving: (1) mafic mineral accumulation at the floor; (2) differentiation, convection and solidification along the walls; (3) storage of differentiated magma at the roof; (4) plume convection; (5) convective self-mixing; (6) redistribution of the exsolved phases. As stated previously (e.g. Huppert *et al.*, 1986; de Silva & Wolff, 1995), the aspect ratio of the chamber plays an important role in magma evolution. The numerical simulations presented in this study emphasize the role of the aspect ratio in the magma fluid dynamics, compositional variations and exsolved phase distribution within a basic reservoir emplaced at shallow depth in the crust. High aspect ratio chambers favor steeper compositional gradients and H_2O gas concentration at the roof. On the other hand, low aspect ratio chambers favor the concentration of the solid phases near the roof and a more pronounced solidification front along the walls. From the simulations provided in this study, it is possible to infer that stock-like chambers would be more eruptible and would exhibit a wider compositional spectrum of eruptive materials than sill-like chambers. Although the simulations are petrologically consistent with processes recognized by petrologists over many decades of field observation, geochemical and mineralogical studies and laboratory results, they are far from reproducing the wide diversity of phenomena identified in nature. We envisage that variations in the initial conditions and/or assumptions of the model open up a wide spectrum of new and exciting possibilities to clarify mafic magma chamber dynamics and their products that can be tested with field and petrological data from natural intrusions. Also, we envisage that the numerical model provided by this study could be adapted to simulate felsic systems, by taking into account the smaller density and temperature contrasts and the higher viscosity with respect to mafic systems. The resulting convective velocities are expected to be significantly lower, particularly if one considers that silicic systems evolve to a cotectic composition after a small amount of undercooling, yielding a dramatic increase in the effective viscosity. Hindered settling would play a more significant role and Darcy's Law for liquid percolation must be included in the simulation. Because the crystal size and the H_2O content in silicic magmas is more significant than in mafic magmas, an approach for determining more accurately the size and shape of crystals and bubbles must also be considered.

ACKNOWLEDGEMENTS

SUPPLEMENTARY DATA

The following space- and time-dependent variables are shown in a set of nine videos available at *Journal of Petrology* online (http://www.petrology.oxfordjournals.org/). The videos are in Flash Player format (swf extension) to be viewed from a web browser.

The following seven videos show the simulations of a stock-like chamber.

Video 1: Temperature (T) of the magma within the chamber and in the surrounding rock.

Video 2: Velocities (u) of magma flow. For a better video visualization, only magnitudes of velocity below 20 m/yr were considered.

Videos 3 and 4: Silica content (SiO2 wt %) in magma and liquid, respectively.

Videos 5 and 6: Mg-number in magma and liquid, respectively.

Video 7: Dispersion parameter (Dϕ) of solid phase suspended in the liquid. Positive/negative values correspond to the excess/depletion (in vol. %) of solids (irrespective of mineral) suspended in the liquid with respect to the amount of solid phase that was crystallized from the same liquid.

A color scale is provided for each variable. Isopleths represent the same values as shown in the color scale for the respective variable. Arrows represent the velocity fields of magma flow normalized to the maximum velocity value obtained in the chamber at a particular moment.

The results of the sill-like chamber simulations are shown in the following two videos.

Video 8: Temperature of the magma and host rock.

Video 9: Silica content in magma.

Brief simulation results of the Lc–Di binary system are also included as Supplementary Data.

REFERENCES

Annen, C., Blundy, J. D. & Sparks, R. S. J. (2006). The genesis of intermediate and silicic magmas in deep crustal hot zones. *Journal of Petrology* **47**, 505–539.

Asimow, P. D. & Ghiorso, M. S. (1998). Algorithmic modifications extending melts to calculate subsolidus phase relations. *American Mineralogist* **83**, 1127–1131.

Bachmann, O. & Bergantz, G. W. (2004). On the origin of crystal-poor rhyolites: extracted from batholithic crystal mushes. *Journal of Petrology* **45**, 1565–1582.

Bachmann, O. & Bergantz, G. W. (2006). Gas percolation in upper-crustal silicic crystal mushes as a mechanism for upward heat advection and rejuvenation of near-solidus magma bodies. *Journal of Volcanology and Geothermal Research* **149**, 85–102.

Bachmann, O. & Bergantz, G. W. (2008). Deciphering magma chamber dynamics from styles of compositional zoning in large silicic ash flow sheets. In: Putirka, K. D. & Tepley, F. J., III (eds) *Minerals, Inclusions and Volcanic Processes. Mineralogical Society of America, Reviews in Mineralogy and Geochemistry* **69**, 651–674.

Barnea, E. & Mizrahi, J. (1973). A generalized approach to the fluid dynamics of particulate systems. Part I. General correlation for fluidization and sedimentation in solid multiparticulate systems. *Chemical Engineering Journal* **5**, 171–189.

Bergantz, G. (1990). Melt fraction diagrams; the link between chemical and transport models. In: Putirka, K. D. & Tepley, F. J., III (eds) *Minerals, Inclusions and Volcanic Processes. Mineralogical Society of America, Reviews in Mineralogy and Geochemistry* **69**, 239–257.

Bergantz, G. W. (1995). Changing techniques and paradigms for the evaluation of magmatic processes. *Journal of Geophysical Research* **100**, 17603–17613.

Bergantz, G. W. (2000). On the dynamics of magma mixing by reintrusion: implications for pluton assembly processes. *Journal of Structural Geology* **22**, 1297–1309.

Bergantz, G. W. & Ni, J. (1999). A numerical study of sedimentation by dripping instabilities in viscous fluids. *International Journal of Multiphase Flow* **25**, 307–320.

Bowen, N. L. (1928). *The Evolution of the Igneous Rocks*. Princeton, NJ: Princeton University Press, 332 pp.

Brandeis, G. & Jaupart, C. (1986). On the interaction between convection and crystallization in cooling magma chambers. *Earth and Planetary Science Letters* **77**, 345–361.

Brandeis, G. & Marsh, B. D. (1989). The convective liquidus in a solidifying magma chamber: a fluid dynamic investigation. *Nature* **339**, 613–616.

Broadwell, J. E. & Mungal, M. G. (1991). Large-scale structures and molecular mixing. *Physics of Fluids A: Fluid Dynamics* **3**, 1193–1206.

Burgisser, A., Bergantz, G. W. & Breidenthal, R. E. (2005). Addressing complexity in laboratory experiments: the scaling of dilute multiphase flows in magmatic systems. *Journal of Volcanology and Geothermal Research* **141**, 245–265.

Cardoso, S. S. & Woods, A. W. (1999). On convection in a volatile-saturated magma. *Earth and Planetary Science Letters* **168**, 301–310.

Carmichael, I. S. E. (2002). The andesite aqueduct: perspective on the evolution of intermediate magmatism in west–central (105°–99°W) Mexico. *Contributions to Mineralogy and Petrology* **143**, 641–663.

Carmichael, I. S. E. (2004). The activity of silica, water and the equilibration of intermediate and silicic magmas. *American Mineralogist* **89**, 1438–1446.

Cawthorn, R. G. & McCarthy, T. S. (1980). Variations in Cr content of magnetite from the upper zone of the Bushveld Complex—evidence for heterogeneity and convection currents in magma chambers. *Earth and Planetary Science Letters* **46**, 335–343.

Cervantes, P. & Wallace, P. J. (2003). Role of H_2O in subduction-zone magmatism: New insights from melt inclusions in high-Mg basalts from central Mexico. *Geology* **31**, 235–238.

Chapman, D. S. & Furlong, K. P. (1992). Thermal state of the continental lower crust. In: Fountain, D. M., Arculus, R. & Kay, R. W. (eds) *Continental Lower Crust. Developments in Geotectonics*. Amsterdam: Elsevier, pp. 179–199.

Chen, C. F. & Turner, J. S. (1980). Crystallization in a double-diffusive system. *Journal of Geophysical Research* **85**, 2573–2593.

Christiansen, E. H. (2005). Contrasting processes in silicic magma chambers: evidence from very large volume ignimbrites. *Geological Magazine* **142**, 669–681.

Clauser, C. & Huenges, E. (1995). *Thermal Conductivity of Rocks and Minerals*. In: Ahrens, T. J. (ed.) *Rock Physics—Phase Relations. A Handbook of Physical Constants*. Washington, DC: American Geophysical Union, pp. 105–126.

Coleman, D. S., Gray, W. & Glazner, A. F. (2004). Rethinking the emplacement and evolution of zoned plutons: Geochronologic evidence for incremental assembly of the Tuolumne Intrusive Suite, California. *Geology* **32**, 443–436.

Cooper, K. M. & Reid, M. R. (2008). Uranium-series crystal ages. In: Putirka, K. D. & Tepley, F. J., III (eds) *Minerals, Inclusions and Volcanic Processes. Mineralogical Society of America, Reviews in Mineralogy and Geochemistry* **69**, 479–544.

Couch, S., Sparks, R. S. J. & Carroll, M. R. (2001). Mineral disequilibrium in lavas explained by convective self-mixing in open magma chambers. *Nature* **411**, 1037–1039.

de Silva, S. L. & Wolff, J. A. (1995). Zoned magma chambers: the influence of magma chamber geometry on sidewall convective fractionation. *Journal of Volcanology and Geothermal Research* **65**, 111–118.

Cox, K. G. & Mitchell, C. (1988). Importance of crystal settling in the differentiation of Deccan Trap basaltic magmas. *Nature* **333**, 447–449.

Dimotakis, P. E. (2005). Turbulent mixing. *Annual Review of Fluid Mechanics* **37**, 329–356.

Einstein, A. (1906). A new determination of molecular dimensions. *Annalen der Physik* **19**, 289–306.

Ghiorso, M. S. & Sack, R. O. (1995). Chemical mass transfer in magmatic processes: IV. A revised and internally consistent thermodynamic model for the interpolation and extrapolation of liquid–solid equilibria in magmatic systems at elevated temperatures and pressures. *Contributions to Mineralogy and Petrology* **119**, 197–212.

Gibb, F. G. F. & Henderson, C. M. B. (1992). Convection and crystal settling in sills. *Contributions to Mineralogy and Petrology* **109**, 538–545.

Gibb, F. G. F. & Henderson, C. M. B. (2006). Chemistry of the Shiant Isles Main Sill, NW Scotland, and wider implications for the petrogenesis of mafic sills. *Journal of Petrology* **47**, 191–230.

Giordano, D. & Dingwell, D. B. (2003). Non-Arrhenian multicomponent melt viscosity: a model. *Earth and Planetary Science Letters* **208**, 337–349.

Glazner, A. F. (1994). Foundering of mafic plutons and density stratification of continental crust. *Geology* **22**, 435–438.

Glazner, A. F., Bartley, J. M., Coleman, D. S., Gray, W. & Taylor, R. Z. (2004). The interpolation and extrapolation of liquid–solid equilibria in magmatic systems at elevated temperatures and pressures. *GSA Today* **14**, 4–11.

Grove, T. L., Parman, S. W., Bowring, S. A., Price, R. S. & Baker, M. B. (2002). The role of an H_2O-rich fluid component in the generation of primitive basaltic andesites and andesites from the Mt. Shasta region, N California. *Contributions to Mineralogy and Petrology* **142**, 375–396.

Gurenko, A. A., Belousov, A. B., Trumbull, R. B. & Sobolev, A. V. (2005). Explosive basaltic volcanism of the Chikurachki Volcano (Kurile arc, Russia): Insights on pre-eruptive magmatic conditions and volatile budget revealed from phenocryst-hosted melt inclusions and groundmass glasses. *Journal of Volcanology and Geothermal Research* **147**, 203–232.

Gutiérrez, F., Gioncada, A., González Ferrán, O., Lahsen, A. & Mazzuoli, R. (2005). The Hudson Volcano and surrounding monogenetic centres (Chilean Patagonia): An example of volcanism associated with ridge–trench collision environment. *Journal of Volcanology and Geothermal Research* **145**, 207–233.

Hawkesworth, C. J., Blake, S., Evans, P., Hughes, R., Macdonald, R., Thomas, L. E., Turner, S. P. & Zellmer, G. (2000). Time scales of crystal fractionation in magma chambers—integrating physical, isotopic and geochemical perspectives. *Journal of Petrology* **41**, 991–1006.

Hess, G. B. (1972). Heat and mass transport during crystallization of the Stillwater Igneous Complex. *Geological Society of America, Memoirs* **132**, 503–520.

Hess, K. U., Dingwell, D. B. & Rössler, E. (1996). Parametrization of viscosity–temperature relations of aluminosilicate melts. *Chemical Geology* **128**, 155–163.

Hildreth, W. & Wilson, C. J. N. (2007). Compositional zoning of the Bishop Tuff. *Journal of Petrology* **48**, 951–999.

Hills, R. N., Loper, D. E. & Roberts, P. H. (1983). A thermodynamically consistent model of a mushy zone. *Quarterly Journal of Mechanics and Applied Mathematics* **36**, 505–540.

Huppert, E. & Sparks, S. (1984). Double-diffusive convection due to crystallization. *Annual Review of Earth and Planetary Sciences* **12**, 11–37.

Huppert, E., Sparks, S., Wilson, R. & Hallworth, M. (1986). Cooling and crystallization at an inclined plane. *Earth and Planetary Science Letters* **79**, 319–328.

Jaupart, C. & Brandeis, G. (1986). The stagnant bottom layer of convecting magma chambers. *Earth and Planetary Science Letters* **80**, 183–199.

Jaupart, C. & Tait, S. (1995). Dynamics of differentiation in magma reservoirs. *Journal of Geophysical Research* **100**, 17615–17636.

Jaupart, C., Brandeis, G. & Allègre, C. J. (1984). Stagnant layers at the bottom of convecting magma chambers. *Nature* **308**, 535–538.

Kahle, A., Winkler, B. & Hennion, B. (2003). Is Faxen's correction function applicable to viscosity measurements of silicate melts with the falling sphere method? *Journal of Non-Newtonian Fluid Mechanics* **111**, 203–215.

Kaneko, K. & Koyaguchi, T. (2004). Experimental study on the effects of crustal temperature and composition on assimilation with fractional crystallization at the floor of magma chambers. *Journal of Volcanology and Geothermal Research* **129**, 155–172.

Koyaguchi, T., Hallworth, M. A., Huppert, H. E. & Sparks, R. S. J. (1990). Sedimentation of particles from a convecting fluid. *Nature* **343**, 447–450.

Krane, M. J. M. & Incropera, F. P. (1996). A scaling analysis of the unidirectional solidification of a binary alloy. *International Journal of Heat and Mass Transfer* **39**, 3567–3579.

Krane, M. J. M. & Incropera, F. P. (1997). Solidification of ternary metal alloys—II. Predictions of convective phenomena and solidification behavior in Pb–Sb–Sn alloys. *International Journal of Heat and Mass Transfer* **40**, 3837–3847.

Krane, M. J. M., Incropera, F. P. & Gaskell, D. R. (1997). Solidification of ternary metal alloys—I. Model development. *International Journal of Heat and Mass Transfer* **40**, 3827–3835.

Krane, M. J. M. (2004). Macrosegregation development during solidification of a multicomponent alloy with free-floating solid particles. *Applied Mathematical Modelling* **28**, 95–107.

Latypov, R. M. (2003a). The origin of basic–ultrabasic sills with S-, D-, and I-shaped compositional profiles by *in situ* crystallization of a single input of phenocryst-poor parental magma. *Journal of Petrology* **44**, 1619–1656.

Latypov, R. M. (2003b). The origin of marginal compositional reversals in basic–ultrabasic sills and layered intrusions by Soret fractionation. *Journal of Petrology* **44**, 1579–1618.

Lejeune, A. M., Bottinga, Y., Trull, T. W. & Richet, P. (1999). Rheology of bubble-bearing magmas. *Earth and Planetary Science Letters* **166**, 71–84.

Lejeune, A. M., Bottinga, Y., Trull, T. W. & Richet, P. (2000). Rheology of bubble-bearing magmas: reply to a critical comment by Spera and Stein. *Earth and Planetary Science Letters* **175**, 333–334.

Le Roux, J. P. (2004). A hydrodynamic classification of grain shapes. *Journal of Sedimentary Research* **74**, 135–143.

Lohmar, S., Robin, C., Gourgaud, A., Clavero, J., Parada, M. Á., Moreno, H., Ersoy, O., López-Escobar, L. & Naranjo, J. A. (2007). Evidence of magma–water interaction during the 13,800 years BP explosive cycle of the Licán Ignimbrite, Villarrica volcano (southern Chile). *Revista Geológica de Chile* **34**, 233–247.

López-Escobar, L., Cembrano, J. & Moreno, H. (1995). Geochemistry and tectonics of the Chilean Southern Andes basaltic Quaternary volcanism (37–46°S). *Revista Geológica de Chile* **22**, 219–234.

Lowenstern, J. B. (1994). Dissolved volatile concentrations in an ore forming magma. *Geology* **10**, 353–367.

Macleod, N. S. & Sherrod, D. R. (1988). Geologic evidence for a magma chamber beneath Newberry Volcano, Oregon. *Journal of Geophysical Research* **93**, 10067–10079.

Manga, M., Castro, J., Cashman, K. V. & Loewenberg, M. (1998). Rheology of bubble-bearing magmas. *Journal of Volcanology and Geothermal Research* **87**, 15–28.

Mahood, G. & Cornejo, P. (1992). Evidence for ascent of differentiated liquids in a silicic magma chamber found in a granitic pluton. *Transactions of the Royal Society of Edinburgh, Earth Sciences* **83**, 63–69.

Marsh, B. D. (1981). On the crystallinity, probability of occurrence, and rheology of lava and magma. *Contributions to Mineralogy and Petrology* **78**, 85–98.

Marsh, B. D. (1996). Solidification fronts and magmatic evolution. *Mineralogical Magazine* **60**, 5–40.

Martin, D., Griffiths, W. & Campbell, I. H. (1987). Compositional and thermal convection in magma chambers. *Contributions to Mineralogy and Petrology* **96**, 465–475.

Matzel, J. E. P., Bowring, S. A. & Miller, R. B. (2006). Time scales of pluton construction at differing crustal levels: Examples from the Mount Stuart and Tenpeak intrusions, North Cascades, Washington. *Geological Society of America Bulletin* **118**, 1412–1430.

McBirney, A. R. (1980). Mixing and unmixing of magmas. *Journal of Volcanology and Geothermal Research* **7**(3/4), 357–371.

McBirney, A. R. & Noyes, R. (1979). Crystallization and layering of the Skaergaard intrusion. *Journal of Petrology* **20**, 487–554.

McBirney, A. R., Baker, B. H. & Nilson, R. H. (1985). Liquid fractionation. Part I: Basic principles and experimental simulations. *Journal of Volcanology and Geothermal Research* **24**, 1–24.

Miyabuchi, Y., Watanabe, K. & Egawa, Y. (2006). Bomb-rich basaltic pyroclastic flow deposit from Nakadake, Aso Volcano, southwestern Japan. *Journal of Volcanology and Geothermal Research* **155**, 90–103.

Morse, S. A. (1982). Igneous petrology. *Science* **217**, 823–824.

Nelson, S. T. & Montana, A. (1992). Sieve-textured plagioclase in volcanic rocks produced by rapid decompression. *American Mineralogist* **77**, 1242–1249.

Murphy, M. D., Sparks, R. S. J., Barclay, J., Carroll, M. R. & Brewer, T. S. (2000). Remobilization of andesite magma by intrusion of mafic magma at the Soufrière Hills Volcano, Montserrat West Indies. *Journal of Petrology* **41**, 21–42.

Ni, J. & Incropera, F. P. (1995a). Extension of the continuum model for transport phenomena occurring during metal alloy solidification—I. The conservation equations. *International Journal of Heat and Mass Transfer* **38**, 1271–1284.

Ni, J. & Incropera, F. P. (1995b). Extension of the continuum model for transport phenomena occurring during metal alloy solidification—II. Microscopic considerations. *International Journal of Heat and Mass Transfer* **38**, 1285–1296.

Oldenburg, C. M. & Spera, F. J. (1990). Simulation of phase change and convection in magma bodies. *Heat Transfer in Earth Science Studies (ASME-HTD)* **149**, 35–42.

Oldenburg, C. M. & Spera, F. J. (1991). Numerical modeling of solidification and convection in a viscous pure binary eutectic system. *International Journal of Heat and Mass Transfer* **34**, 2107–2121.

Oldenburg, C. M. & Spera, F. J. (1992a). Hybrid model for solidification and convection. *Numerical Heat Transfer* **B21**, 217–229.

Oldenburg, C. M. & Spera, F. J. (1992b). Modeling transport processes in nonlinear systems: The example of solidification and convection. *Chaotic Processes in the Geological Sciences: IMA Volume in Mathematics and its Applications* **41**, 221–232.

Oldenburg, C. M., Spera, F. J., Yuen, D. A. & Sewell, G. (1989). Dynamic mixing in magma bodies: theory, simulations, and implications. *Journal of Geophysical Research* **94**, 9215–9236.

Pal, R. (2003). Rheological behavior of bubble-bearing magmas. *Earth and Planetary Science Letters* **207**, 165–179.

Parada, M. A., Féraud, G., Fuentes, F., Aguirre, L., Morata, D. & Larrondo, P. (2005). Ages and cooling history of the Early Cretaceous Caleu pluton: testimony of a switch from a rifted to a compressional continental margin in central Chile. *Journal of the Geological Society, London* **162**, 273–287.

Petford, N. (1996). Dykes or diapirs? *Transactions of the Royal Society of Edinburgh: Earth Sciences* **87**, 105–114.

Petford, N. (2003). Rheology of granitic magmas during ascent and emplacement. *Annual Review of Earth and Planetary Sciences* **31**, 399–427.

Petford, N. (2009). Which effective viscosity? *Mineralogical Magazine* **73**, 167–191.

Pichavant, M., Mysen, B. O. & Macdonald, R. (2002). Source and H_2O content of high-MgO magmas in island arc settings: an experimental study of a primitive calc-alkaline basalt from St. Vincent, Lesser Antilles arc. *Geochimica et Cosmochimica Acta* **66**, 2193–2209.

Pinkerton, H. & Stevenson, R. J. (1992). Methods of determining the rheological properties of magmas at sub-liquidus temperatures. *Journal of Volcanology and Geothermal Research* **53**, 47–66.

Pitcher, W. S. (1978). The anatomy of a batholith. *Journal of the Geological Society, London* **135**, 157–182.

Putirka, K. D. (2008). Introduction. In: Putirka, K. D. & Tepley, F. J., III (eds) *Minerals, Inclusions and Volcanic Processes. Mineralogical Society of America, Reviews in Mineralogy and Geochemistry* **69**, 1–8.

Raia, F. & Spera, F. J. (1997). Simulations of crustal anatexis: Implications for the growth and differentiation of continental crust. *Journal of Geophysical Research* **102**(B10), 22629–22648.

Rao, R., Mondy, L., Sun, A. & Altobelli, S. (2002). A numerical and experimental study of batch sedimentation and viscous resuspension. *International Journal for Numerical Methods in Fluids* **39**, 465–483.

Rao, R. R., Mondy, L. A. & Altobelli, S. A. (2007). Instabilities during batch sedimentation in geometries containing obstacles: A numerical and experimental study. *International Journal for Numerical Methods in Fluids* **55**, 723–735.

Roscoe, R. (1952). The viscosity of suspensions of rigid spheres. *Annalen der Physik* **3**, 267–269.

Rüpke, L. H. & Hort, M. (2004). The impact of side wall cooling on the thermal history of lava lakes. *Journal of Volcanology and Geothermal Research* **131**, 165–178.

Ruprecht, P., Bergantz, G. W. & Dufek, J. (2008). Modeling of gas-driven magmatic overturn: Tracking of phenocryst dispersal and gathering during magma mixing. *Geochemistry, Geophysics, Geosystems* **9**, 1–20.

Russell, J. K., Giordano, D. & Dingwell, D. B. (2003). High-temperature limits on viscosity of non-Arrhenian silicate melts. *American Mineralogist* **88**, 1390–1394.

Sepúlveda, F., Dorsch, K., Lahsen, A., Bender, S. & Palacios, C. (2004). Chemical and isotopic composition of geothermal discharges from the Puyehue–Cordón Caulle area (40·5°S), Southern Chile. *Geothermics* **33**, 655–673.

Shaw, H. R. (1965). Comments on viscosity, crystal settling, and convection in granitic magmas. *American Journal of Science* **263**, 120–152.

Shinohara, H., Kohei, K. & Lowenstern, J. (1995). Volatile transport in a convecting magma column: Implications for porphyry Mo mineralization. *Geology* **23**, 1091–1094.

Sisson, T. W. & Grove, T. L. (1993). Experimental investigations of the role of H_2O in calc-alkaline differentiation and subduction zone magmatism. *Contributions to Mineralogy and Petrology* **113**, 143–166.

Sisson, T. W., Ratajeski, K., Hankins, W. B. & Glazner, A. F. (2005). Voluminous granitic magmas from common basaltic sources. *Contributions to Mineralogy and Petrology* **148**, 635–661.

Sparks, R. S. J. & Huppert, H. E. (1984). Density changes during the fractional crystallization of basaltic magmas: fluid dynamic implications. *Contributions to Mineralogy and Petrology* **85**, 300–309.

Sparks, R. S. J., Meyer, P. & Sigurdsson, H. (1980). Density variation amongst mid-ocean ridge basalts: implications for magma mixing and the scarcity of primitive basalts. *Earth and Planetary Science Letters* **46**, 419–430.

Sparks, R. S. J., Huppert, H. E. & Turner, J. S. (1984). The fluid dynamics of evolving magma chambers. *Philosophical Transactions of the Royal Society of London, Part A* **310**, 511–534.

Spera, F. J. (2000). Physical properties of magma. In: Sigurdsson, H. (ed.) *Encyclopedia of Volcanoes*. New York: Academic Press, pp. 171–190.

Spera, F. J. & Stein, D. J. (2000). Comment on 'Rheology of bubble-bearing magmas' by Lejeune *et al*. *Earth and Planetary Science Letters* **175**, 327–331.

Spera, F. J., Yuen, D. A. & Kemp, D. V. (1984). Mass transfer rates along vertical walls in magma chambers and marginal upwelling. *Nature* **310**, 764–767.

Spera, F. J., Oldenburg, C. M., Christensen, C. & Todesco, M. (1995). Simulations of convection with crystallization in the system $KAlSi_2O_6$–$CaMgSi_2O_6$; implications for compositionally zoned magma bodies. *American Mineralogist* **80**, 1188–1207.

Stein, D. J. & Spera, F. J. (2002). Shear viscosity of rhyolite–vapor emulsions at magmatic temperatures by concentric cylinder rheometry. *Journal of Volcanology and Geothermal Research* **113**, 243–258.

Stolper, E. (1982). Water in silicate glasses: An infrared spectroscopic study. *Contributions to Mineralogy and Petrology* **81**, 1–17.

Tait, S. R. & Jaupart, C. (1996). The production of chemically stratified and adcumulate plutonic igneous rocks. *Mineralogical Magazine* **60**, 99–114.

Tait, S. R., Huppert, H. E. & Sparks, R. S. J. (1984). The role of compositional convection in the formation of adcumulate rocks. *Lithos* **17**, 139–146.

Thomas, N., Tait, S. & Koyaguchi, T. (1993). Mixing of stratified liquids by the motion of gas bubbles: application to magma mixing. *Earth and Planetary Science Letters* **115**, 161–175.

Trial, A. & Spera, F. J. (1990). Mechanisms for the generation of compositional heterogeneities in magma chambers. *Geological Society of America Bulletin* **102**, 353–367.

Turner, J. S. (1980). A fluid-dynamical model of differentiation and layering in magma chambers. *Nature* **285**, 213–215.

Turner, J. S. & Gustafson, L. B. (1981). Fluid motions and compositional gradients produced by crystallization or melting at vertical boundaries. *Journal of Volcanology and Geothermal Research* **11**, 93–125.

Wiebe, R. A., Manon, M. R., Hawkins, D. P. & McDonough, W. F. (2004). Late-stage mafic injection and thermal rejuvenation of the Vinalhaven Granite, coastal Maine. *Journal of Petrology* **45**, 2133–2153.

Williams, S. N. (1983). Plinian airfall deposits of basaltic composition. *Geology* **11**, 211–214.

Wolff, J. A., Wörner, G. & Blake, S. (1990). Gradients in physical parameters in zoned felsic magma bodies: Implications for evolution and eruptive withdrawal. *Journal of Volcanology and Geothermal Research* **43**, 37–55.

Zhang, K. & Acrivos, A. (1994). Viscous resuspension in fully developed laminar pipe flows. *International Journal of Multiphase Flow* **20**, 579–591.

APPENDIX A

We used the Multiphysics software R.3.4a to obtain the solution of the governing equations by the finite-element method (FEM). FEM is a computational method that subdivides an object into very small finite-size elements. Each element is assigned to a set of characteristic equations, which are then solved as a set of simultaneous equations to predict the object behavior. The mesh of elements is constituted by more than 10,000 triangular finite elements using a static mesh, or Eulerian description. The linear system solution is obtained with the UMFPACK direct solver. It solves general systems of the form $Ax = b$ using the unsymmetric-pattern multifrontal method and direct LU factorization of the sparse matrix A ($A = LU$). It employs COLAMD and AMD approximate minimum degree preordering algorithms to permute the columns so that the fill-in is minimized. The code, written in C, uses level-3 BLAS (Basic Linear Algebra Subprograms) for optimal performance. COMSOL Multiphysics uses UMFPACK version 4.2 written by T. A. Davis (http://www.cise.ufl.edu/research/sparse/umfpack). For time differential variables the relative tolerance is 10^{-4}, and the absolute tolerance is 10^{-5} km/yr for velocities (u and v), 10^{-2}°C for temperatures (T and Tr), and 10^{-2} vol. % for the phase contents. The model fails to converge where flow velocities exceed 300 m/yr. Because of the incompressible character of the magma assumed in the model, pressure remains lithostatic and no absolute tolerance is assigned. The minimum finite element quality, defined as $q = 43\sqrt{A}/(h1^2 + h2^2 + h3^2$ (A and h are the area and the side length of each triangular finite element, respectively), is 0·53. The shape function variables are Lagrange finite elements of linear order for pressure, quadratic order for velocities and phases contents, and cubic order for temperatures. A coefficient of isotropic artificial diffusion using a tuning parameter of 0·25 is added to the phase equations to prevent the propagation of oscillation effects to other parts of the system. The solution time of the simulation depends on computational facilities. For example, using a PC with AMD 64 (3·2 GHz) processor and 8 GB of RAM using the Linux (Open Suse v10.1) operating system the simulation takes about 18 days.

APPENDIX B

To facilitate the solution of the equations we introduce the following dimensionless characteristic variables:

$x = \mathrm{x}/\underline{\mathrm{L}}$ (distance)
$m = \mathrm{m}/\underline{\mathrm{M}}$ (mass)
$t = \mathrm{t}/\underline{\mathrm{T}}$ (time).
$\underline{\mathrm{L}}$, $\underline{\mathrm{M}}$ and $\underline{\mathrm{T}}$ are the following constants:
$\underline{\mathrm{L}} = 1000\,\mathrm{m} = 1\,\mathrm{km}$
$\underline{\mathrm{M}} = 2\cdot51 \times 10^{-12}\,\mathrm{kg}$
$\underline{\mathrm{T}} = 3\cdot154 \times 10^7\,\mathrm{s} = 1\,\mathrm{year}.$

Temperature, composition and phase volume fraction were not normalized; consequently, these variables were calculated in Kelvin, wt %, and vol. fraction, respectively.

By substituting the dimensionless characteristic variables in the partial differentiation equations, the following normalizing δ factors were obtained for the heat transfer, phase exsolution, and incompressible Navier–Stokes equations [equations (1), (6) and (13) in the text]:

$$\delta_T = \underline{M}/\underline{L}\,\underline{T}^3 = 8\cdot003 \times 10^{-14}$$
$$\delta_\phi = 1/\underline{T} = 3\cdot171 \times 10^{-8}$$

$$\delta_u = \underline{M}/\underline{L}^2\,\underline{T}^2 = 2\cdot524 \times 10^{-9}.$$

APPENDIX C

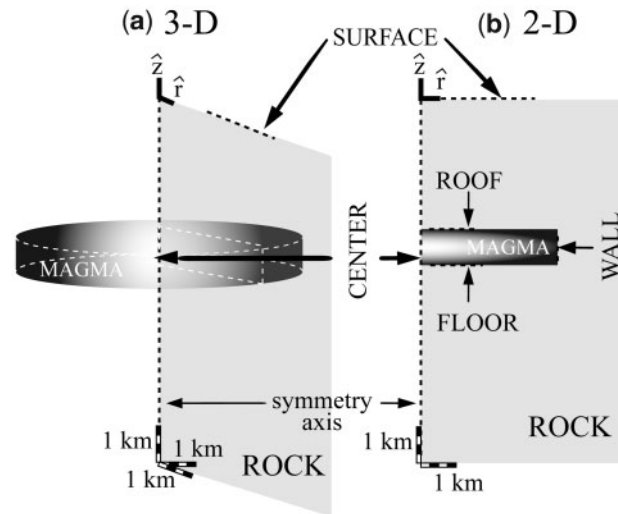The geometry of the sill-like magma chamber is shown in Fig. A1.

Fig. A1. Geometry of the sill-like magma chamber: (a) cylindrical magma chamber of 50 km^3 simulating a sill-like body; (b) cross-section of the right half of the magma chamber that is used to show the experiment results in Figs 6–8 and the videos.